UNIFIED MULTI-MATERIAL TOPOLOGY OPTIMIZATION OF HETEROGENEOUS STRUCTURES FOR THREE-PHASE MULTI-PHYSICS SYSTEMS

Nhan T. Dang[a,b], Qui X. Lieu[a,b], Thanh T. Banh[c,d,*]

[a]*Faculty of Civil Engineering, Ho Chi Minh City University of Technology (HCMUT), 268 Ly Thuong Kiet street, Dien Hong ward, Ho Chi Minh City, Vietnam*
[b]*Vietnam National University Ho Chi Minh City (VNU-HCM), Linh Xuan ward, Ho Chi Minh City, Vietnam*
[c]*Mechanical System Engineering, Jeonbuk National University, 567, Baekje-daero, Deokjin-gu, Jeonju-si, Jeollabuk-do 54896, Republic of Korea*
[d]*Graduate School of Mechanical-Aerospace-Electric Convergence Engineering, Jeonbuk National University, 567, Baekje-daero, Deokjin-gu, Jeonju-si, Jeollabuk-do 54896, Republic of Korea*

Article history:
Received 16/01/2026, Revised 25/6/2026, Accepted 26/6/2026

Abstract

While structural topology optimization is a useful tool for multiphysics designs, most existing studies focus on homogeneous material configurations, with limited attention given to heterogeneous systems. To address this limitation, this paper proposes a unified topology optimization framework for heterogeneous structures - specifically Functionally Graded Materials (FGMs) - under triply coupled thermal, mechanical, and design-dependent pressure loads. Unlike traditional discrete multi-material approaches, the proposed methodology utilizes the continuous spatial variation of material properties using an explicit power-law interpolation scheme. The model integrates a sequential thermo-mechanical coupling strategy with a Darcy-based representative solid-phase model to evaluate design-dependent pressure fields. This allows for a consistent treatment of the interactions among thermal effects, mechanical responses, and evolving pressure loads. Several numerical examples are presented to verify the accuracy and efficiency of the proposed approach. Furthermore, a comparison demonstrates that FGM designs provide improved structural performance over conventional homogeneous layouts in three-phase multiphysics environments. This shows their applicability in engineering practice

Keywords: multi-materials; topology optimization; three-phase thermo-mechanical-pressure systems; design dependent load; heterogeneous materials; functionally graded materials (FGM)

https://doi.org/10.31814/stce.huce2026-20(3)-05

1. Introduction

Traditional structural design methods often lead to the poor use of the material. Recent developments in digital production, though, brought up a robust interest in topology optimization (TO) as an effective mechanism for arranging materials in the highest possible order [1–5]. Drawing on these improvements, multi-material topology optimization (MTO) has generated significant interest because of the increased freedom in the design. Thus, various methodological frameworks have been defined and successfully applied for different engineering problems [6–25]. Herein, the material distribution is modeled by the generalized SIMP (GSIMP) approach [18, 22] which offers a flexible and stable basis for modeling heterogeneous material layouts. Further, the polygonal finite element method is used as a unified discretization framework in the proposed topology optimization formulation to further enhance geometric flexibility [26]

*Corresponding author. *E-mail address:* btthanhg16@jbnu.ac.kr (Banh, T. T.)

FGMs, from a materials point of view, have risen as a viable substitute for discrete multi-material designs. Fitting microstructural changes that smooth out across spatial coordinates, FGMs reduce the issues with abrupt interfaces between material, and have been the subject of intensive research in the field of modeling and optimization [17, 23, 27–32]. Practically, this high degree of customization of local material properties makes FGMs quite attractive for high performance multiphysics systems. In contemporary engineering applications, various structural components are often subjected to an arbitrary mix of mechanical loads, large thermal fields, and fluid-induced pressures. With such operating conditions pressure applied to boundaries is typically design-dependent. By ignoring this natural coupling or thermal expansion behavior, the structural results can be predicted wrongly for the structure and reliability can be jeopardized

Several parameterization options have also been suggested to tackle the design-related pressure problems [33–38]. Of these, the robust model proposed by Kumar et al. [39–42], in which Darcy's law (augmented) by a drainage term was exploited. This enables one to efficiently assess design-dependent pressure loads and their sensitivities, avoiding establishing evolving boundaries explicitly, making for natural compatibility with density-based TO frameworks

Inspired by the above problems, this work presents an interdependent TO model in order to handle heterogeneous configurations subjected to coupled thermal-mechanical-pressure loadings. In particular, our research questions include: (1) How can continuous FGM interpolation, design-dependent pressure loads, and steady-state thermoelastic behavior be consistently incorporated in one density-based topology optimization model? (2) To what extent does the continuous FGM layout improve structural compliance compared to conventional discrete multi-material configurations under these specific three-phase multiphysics conditions? It is essential to specify the overall scope and assumptions of the proposed framework. The present formulation is strictly confined to 2D steady-state linear elasticity under a weak thermo-mechanical coupling assumption. Thus, it does not take into account 3D spatial effects, dynamic structural responses, geometric or material nonlinearities, and particular additive manufacturing limitations. Furthermore, the characterization of heterogeneous materials in this study relies solely on a single explicit exponential interpolation law for FGM modeling

The remainder of this paper is organized as follows. Section 2 presents the governing thermoelastic equations and the modeling of design-dependent pressure loads. Section 3 introduces the FGM interpolation strategy and formulates the optimization problem. Section 4 derives the corresponding sensitivity expressions required for the MMA optimizer. Section 5 presents a series of numerical examples to assess the proposed framework. Finally, Section 6 summarizes the main conclusions

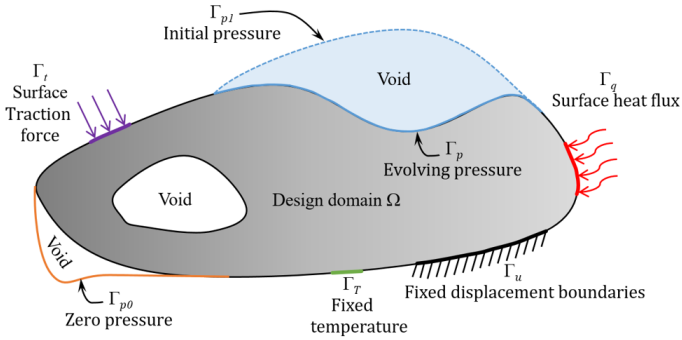

Figure 1. An illustration of how a three-phase multi-physics system behaves when subjected to a range of different loads and boundary conditions

2. Fundamental formulation

This section outlines the governing formulation of the three-phase thermal-mechanical-pressure problem underlying the proposed topology optimization framework. The presentation begins with the coupled thermo-mechanical model, proceeds to the treatment of design-dependent pressure loading, and concludes with the modeling of functionally graded material behavior

2.1. Heat conduction problem

This study adopts a weak thermo-mechanical coupling assumption, wherein the temperature field induces mechanical displacement, but the reverse feedback is negligible [43]. Consequently, the steady-state heat conduction problem without internal heat sources can be solved independently, governed by:

$$\partial_x(k_x\partial_x T) + \partial_y(k_y\partial_y T) = 0 \tag{1}$$

where k_x and k_y denote the anisotropic thermal conductivities of the material. The problem is fully defined by the Dirichlet fixed temperature boundary condition: $T|_{\Gamma_T} = T_0$ on the boundary Γ_T with a prescribed temperature value T_0; and the Neumann surface heat flux: $(k_x\partial_x T n_x + k_y\partial_y T n_y)|_{\Gamma_q} = q_0$, where n_x and n_y are the components of the outward unit normal vector $\boldsymbol{n} = (n_x, n_y)$ perpendicular to the boundary surface, and q_0 is the prescribed heat flux value specifying the amount of heat passing through the boundary Γ_q.

To solve Eq. (1) numerically, the Galerkin method is used to construct the integral weak form over an element's domain Ω_e:

$$\int_{\Omega_e} \left(k_x\partial_x T^e\partial_x\phi_i^e + k_y\partial_y T^e\partial_y\phi_i^e\right) dxdy = \int_{\Gamma_q^e} \phi_i^e q_0\, ds \tag{2}$$

where T^e is the temperature of the element and ϕ_i^e is the shape function associated with node i of the element. The temperature field T^e of each element is approximated as follows:

$$T^e(x,y) = \sum_{j=1}^{N_v} T_j^e \cdot \phi_j^e(x,y) = \boldsymbol{\phi}^e\mathbf{T}^e \tag{3}$$

where N_v is the number of vertices inside the polygonal element.

Since the computational domain is discretized using polygonal elements, Wachspress shape functions [26] are employed to ensure continuity between elements:

$$\begin{aligned} \phi_i^e(\xi) &= \frac{w_i(\xi)}{\sum_{j=1}^{N_v} w_j(\xi)} \\ w_i(\boldsymbol{\xi}) &= \frac{A(\mathbf{p}_{i-1}, \mathbf{p}_i, \mathbf{p}_{i+1})}{A(\mathbf{p}_{i-1}, \mathbf{p}_i, \boldsymbol{\xi})\, A(\mathbf{p}_i, \mathbf{p}_{i+1}, \boldsymbol{\xi})} \end{aligned} \tag{4}$$

where $w_i(\xi)$ is the weight function; A denotes the area of the triangle formed by its three argument points; $\mathbf{p}$ represents the coordinates of the i-th vertex; and $\boldsymbol{\xi}$ is an arbitrary evaluation point within the polygonal element.

After substituting the interpolation expression (3) into the weak form (2), we obtain the system of linear algebraic equations for the thermal problem:

$$\mathbf{K}_{th}\mathbf{T} = \mathbf{F}_{th} \tag{5}$$

where $\mathbf{T}$ is the global nodal temperature vector; $\mathbf{F}_{th}$ is the global thermal load vector, $\mathbf{F}_{th} = \wedge_e \mathbf{F}^e_{th}$ and $\mathbf{K}_{th}$ is the global conductivity matrix, $\mathbf{K}_{th} = \wedge_e \mathbf{K}^e_{th}$.

$\mathbf{K}_{th}$ is assembled from the elemental conductivity matrices $\mathbf{K}^e_{th}$:

$$\mathbf{K}^e_{th} = \int_{\Omega_e} \left(\mathbf{B}^e_{th}\right)^T \mathbf{D}_{th} \mathbf{B}^e_{th}\, dxdy \tag{6}$$

The two matrices in the integral expression (6) are the conductivity matrix $\mathbf{D}_{th}$ and the thermal-strain relation matrix $\mathbf{B}^e_{th}$ (which includes the derivatives of the shape functions):

$$\begin{aligned} \mathbf{D}_{th}\left(k_x, k_y\right) &= \begin{bmatrix} k_x & 0 \\ 0 & k_y \end{bmatrix} \\ \mathbf{B}^e_{th} &= \begin{bmatrix} \partial_x \phi^e_1 & \partial_x \phi^e_2 & \cdots & \partial_x \phi^e_{N_v} \\ \partial_y \phi^e_1 & \partial_y \phi^e_2 & \cdots & \partial_y \phi^e_{N_v} \end{bmatrix} \end{aligned} \tag{7}$$

The elemental thermal load vector $\mathbf{F}^e_{th}$ is defined as follows:

$$\mathbf{F}^e_{th} = \int_{\Gamma^e_q} \boldsymbol{\phi}^T q_0\, d\Gamma \tag{8}$$

2.2. Coupled thermo-mechanical problem

Once the thermal problem (5) is solved to obtain the temperature field T^e, the subsequent objective is to solve the mechanical problem to find the displacement field $\mathbf{U}$. This requires establishing the global force equilibrium equation:

$$\mathbf{KU} = \mathbf{F}_m + \mathbf{F}_\epsilon \tag{9}$$

where $\mathbf{K}$ is the global stiffness matrix, $\mathbf{K} = \wedge_e \mathbf{K}^e$; $\mathbf{F}_m$ is the mechanical load vector, $\mathbf{F}_m = \wedge_e \mathbf{F}^e_m$; and $\mathbf{F}_\epsilon$ is the equivalent nodal force vector induced by thermal expansion, $\mathbf{F}_\epsilon = \wedge_e \mathbf{F}^e_\epsilon$.

The elemental stiffness matrix $\mathbf{K}^e$ describes the resistance of an element to deformation and is computed by:

$$\mathbf{K}^e = \int_{\Omega_e} \mathbf{B}^{eT} \mathbf{D} \mathbf{B}^e\, dxdy \tag{10}$$

where $\mathbf{B}^e$ is the elemental strain-displacement matrix and $\mathbf{D}$ is the elasticity matrix for plane stress:

$$\begin{aligned} \mathbf{B}^e &= \begin{bmatrix} \partial_x \phi^e_1 & 0 & \partial_x \phi^e_2 & 0 & \cdots & \partial_x \phi^e_{N_v} & 0 \\ 0 & \partial_y \phi^e_1 & 0 & \partial_y \phi^e_2 & \cdots & 0 & \partial_y \phi^e_{N_v} \\ \partial_y \phi^e_1 & \partial_x \phi^e_1 & \partial_y \phi^e_2 & \partial_x \phi^e_2 & \cdots & \partial_y \phi^e_{N_v} & \partial_x \phi^e_{N_v} \end{bmatrix} \\ \mathbf{D}\left(E, \nu\right) &= \frac{E}{1-\nu^2} \begin{bmatrix} 1 & \nu & 0 \\ \nu & 1 & 0 \\ 0 & 0 & (1-\nu)/2 \end{bmatrix} \end{aligned} \tag{11}$$

where E is Young's Modulus and ν is Poisson's Ratio.

The equivalent nodal forces, which are converted from external mechanical loads can be expressed as:

$$\mathbf{F}^e_m = \mathbf{F}^e_t + \mathbf{F}^e_b \tag{12}$$

where $\mathbf{F}_t^e$ is the surface traction vector and $\mathbf{F}_b^e$ is the body force vector, defined as follows:

$$\begin{aligned} \mathbf{F}_t^e &= \int_{\Gamma^e} \widetilde{\boldsymbol{\phi}}^T \boldsymbol{t}\, dA \\ \mathbf{F}_b^e &= \int_{\Omega^e} \widetilde{\boldsymbol{\phi}}^T \boldsymbol{b}\, dV \end{aligned} \tag{13}$$

where $\boldsymbol{t}$ is the surface traction vector applied on the boundary Γ^e of the element; $\boldsymbol{b}$ is the body force vector acting over the domain Ω^e of the element; and $\widetilde{\boldsymbol{\phi}}$ is the matrix of shape functions, $\widetilde{\boldsymbol{\phi}} = [\phi_1\mathbf{I}, \phi_2\mathbf{I}, \ldots, \phi_{N_v}\mathbf{I}]$, with $\mathbf{I}$ being the identity matrix.

The thermal load $\mathbf{F}_\epsilon$ originates from the thermal strains $\boldsymbol{\epsilon}_0$, which are calculated based on the temperature difference relative to the reference temperature T_{ref}:

$$\boldsymbol{\epsilon}_0 = \beta \begin{Bmatrix} 1 & 1 & 0 \end{Bmatrix}^T \left[\boldsymbol{\phi}^e \mathbf{T}^e - T_{ref} \right] \tag{14}$$

where β is the thermal expansion coefficient.

According to the standard finite element formulation, the elemental thermal force vector $\mathbf{F}_\epsilon^e$ is computed by integrating the equivalent thermal stress over the element domain:

$$\mathbf{F}_\epsilon^e = \int_{\Omega_e} \mathbf{B}^{eT} \mathbf{D} \boldsymbol{\epsilon}_0\, dxdy \tag{15}$$

To simplify the sensitivity analysis, which is rendered highly complex by the dependencies on E, ν and β; a generalized thermal stress coefficient (TSC) is employed. According to Ref. [44], this parameter consolidates all three material properties into a single quantity, $\gamma = E\beta/(1-\nu)$:

$$\mathbf{F}_\epsilon^e = \gamma \int_{\Omega_e} \mathbf{B}^{eT} \begin{Bmatrix} 1 & 1 & 0 \end{Bmatrix}^T \boldsymbol{\phi}^e \left(\mathbf{T}^e - T_{ref} \mathbf{1}^e \right) dxdy \tag{16}$$

where $\mathbf{1}^e = \begin{Bmatrix} 1 & 1 & \ldots & 1 \end{Bmatrix}^{\mathrm{T}} \in \mathbb{R}^{N_v \times 1}$ defines a column vector containing exactly N_v elements, all of which are equal to 1.

For a more compact representation, we define an elemental combination matrix $\mathbf{C}^e$, which depends solely on the element geometry:

$$\mathbf{C}^e = \int_{\Omega_e} \mathbf{B}^{eT} \begin{Bmatrix} 1 & 1 & 0 \end{Bmatrix}^T \boldsymbol{\phi}^e\, dxdy \tag{17}$$

This allows the representation of the thermal strain load in its final form:

$$\mathbf{F}_\epsilon^e = \gamma \mathbf{C}^e \left(\mathbf{T}^e - T_{ref} \mathbf{1}^e \right) \tag{18}$$

2.3. Modeling of design-dependent pressure loads

To handle design-dependent pressure loads on continuously evolving boundaries, a continuous pressure field (p) is defined over the entire design domain, eliminating the need for explicit boundary tracking. The domain is modeled as a porous medium where void regions ($\alpha_1 \approx 0$) possess high permeability for pressure transmission, while solid regions ($\alpha_1 \approx 1$) have near-zero permeability to block flow. In this formulation, $\boldsymbol{\alpha}_1$ [22] denotes the representative solid-phase vector, as detailed in Section 3.

This approach is realized through two key components: Darcy's law and an additional drainage term. Darcy's law [40, 42] is employed to model the transport of pressure within the porous medium, governing how the pressure field propagates through regions of varying permeability:

$$\boldsymbol{q} = -K(\boldsymbol{\alpha}_1)\nabla p \tag{19}$$

where $\boldsymbol{q}$ is the flux; ∇p is the pressure gradient; and $K(\boldsymbol{\alpha}_1)$ is the permeability coefficient. This is the key component linking the flow to the design. To enable $K(\boldsymbol{\alpha}_1)$ to function as a solid/void switch, it is interpolated using a Heaviside function (H):

$$K(\alpha_1^e) = k_v - (k_v - k_s)H(\alpha_1^e, \eta_k, \beta_k) \tag{20}$$

where α_1^e is the filtered design variable of element e; k_v is the high permeability of the void region; k_s is the extremely low permeability of the solid region, $k_s = 10^{-7}k_v$ [40]; and the function H acts as a switch that transitions the value of K from k_v to k_s as α_1^e crosses a threshold η_k:

$$H\left(\alpha_1^e, \eta_k, \beta_k\right) = \frac{\tanh\left(\beta_k\eta_k\right) + \tanh\left(\beta_k\left(\alpha_1^e - \eta_k\right)\right)}{\tanh\left(\beta_k\eta_k\right) + \tanh\left(\beta_k\left(1 - \eta_k\right)\right)} \tag{21}$$

wherein η_k is the threshold parameter determining the transition location between solid and void states, and β_k controls the steepness of the projection.

According to Kumar et al. [40], employing only Darcy's Law is insufficient, as it may fail to produce a distinct pressure drop at the boundary. To address this, a drainage term (Q_d) is incorporated:

$$Q_d = -D\left(\boldsymbol{\alpha}_1\right)\left(p - p_{ext}\right) \tag{22}$$

where Q_d is the drainage term, representing the volumetric pressure drop occurring per unit volume of the solid material; p is the continuous pressure field at the point under consideration; p_{ext} is the external ambient pressure, $p_{ext} = 0$; and $D(\boldsymbol{\alpha}_1)$ is the drainage coefficient:

$$D(\alpha_1^e) = h_s H(\alpha_1^e, \eta_h, \beta_h) \tag{23}$$

where $H(\alpha_1^e, \eta_h, \beta_h)$ is the Heaviside function with threshold η_h and steepness β_h; and h_s is the solid drainage coefficient controlling the pressure penetration layer thickness:

$$h_s = k_s(\ln\ r/\nabla s)^2 \tag{24}$$

where r is the ratio of the inlet pressure at a depth ∇s, satisfying the condition $p|_{\nabla s} = p_{in}$ [42].

Combining both mechanisms, the final flow equilibrium equation is:

$$\nabla \cdot \boldsymbol{q} - Q_d = 0 \tag{25}$$

Upon FEM discretization, this equation becomes a matrix system for the global pressure vector $\mathbf{P}$:

$$\left(\mathbf{K}_p + \mathbf{K}_{Dp}\right)\mathbf{P} = 0 \tag{26}$$

where $\mathbf{K}_p$ is the flow matrix from Darcy's Law and $\mathbf{K}_{Dp}$ is the matrix from the Drainage Term:

$$\begin{aligned} \mathbf{K}_p^e\left(\boldsymbol{\alpha}_1\right) &= \int_{\Omega_e} K\left(\alpha_1^e\right)\hat{\mathbf{B}}^{eT}\hat{\mathbf{B}}^e\, dxdy \\ \mathbf{K}_{Dp}^e\left(\boldsymbol{\alpha}_1\right) &= \int_{\Omega_e} D\left(\alpha_1^e\right)\boldsymbol{\phi}^{eT}\boldsymbol{\phi}^e\, dxdy \end{aligned} \tag{27}$$

where $\hat{\mathbf{B}}^{eT} = \nabla\boldsymbol{\phi}^{e}$.

After solving Eq. (26) to obtain the pressure field $\mathbf{P}$, it must be converted into a mechanical force vector ($\mathbf{F}_m^e$) to be applied to the structure. Reference [40] demonstrated that the force generated by the pressure field can be represented as an equivalent body force. This equivalent force is defined as $\boldsymbol{b}\,dxdy = -\hat{\mathbf{B}}^{e}\mathbf{P}^{e}\,dxdy$. Based on this equivalency, Eq. (12) is adjusted and rewritten as follows:

$$\mathbf{F}_m^e = \mathbf{F}_t^e - \mathbf{H}^e\mathbf{P}^e \tag{28}$$

where $\mathbf{F}_t^e$ is the elemental fixed traction load and $\mathbf{H}^e$ is the elemental conversion matrix used to compute the equivalent forces from the elemental pressure field $\mathbf{P}^e$:

$$\mathbf{H}^e = \int_{\Omega^e} \widetilde{\boldsymbol{\phi}}^{T}\hat{\mathbf{B}}^{e}\,dxdy \tag{29}$$

2.4. Overall material properties

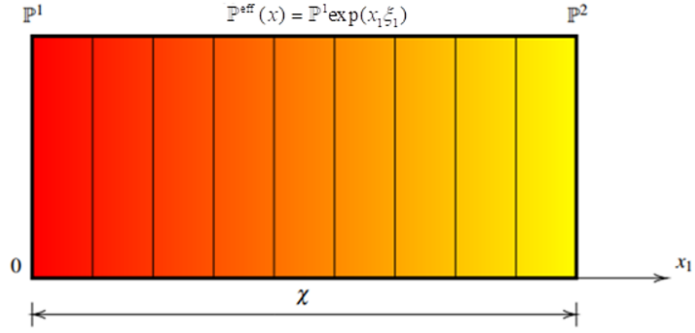

Figure 2. FGM material model graded in the x_1-direction

Functionally graded materials (FGMs) exhibit smoothly varying spatial properties, which mitigate stress concentrations associated with abrupt interfaces. Within the finite element framework, the macroscopic behavior of these heterogeneous materials is efficiently characterized by evaluating their effective properties at the element level. Specifically, the spatial variation of these effective properties at position $\boldsymbol{x} = (x_1, x_2)$ is governed by the exponential law [23, 29, 30, 45]:

$$\mathbb{P}^{eff}(\mathbb{P}^1, \mathbb{P}^2, \boldsymbol{x}) = \mathbb{P}^1 \exp(x_1\xi_1 + x_2\xi_2) \tag{30}$$

where $\mathbb{P}^{eff}(\boldsymbol{x})$ is the effective property at coordinate $\boldsymbol{x} = (x_1, x_2)$; $\mathbb{P}^1$ and $\mathbb{P}^1$ denote the properties of the reference and second base materials, respectively; and the coefficients ξ_1 and ξ_1, which govern the spatial variation rate and direction, are determined by the base properties and two gradient control parameters:

$$\begin{aligned} \xi_1 &= \cos(\theta_m)\,\frac{1}{\chi}\ln\left(\frac{\mathbb{P}^2}{\mathbb{P}^1}\right) \\ \xi_2 &= \sin(\theta_m)\,\frac{1}{\chi}\ln\left(\frac{\mathbb{P}^2}{\mathbb{P}^1}\right) \end{aligned} \tag{31}$$

where χ is the hierarchical length parameter, representing the distance over which the material properties primarily transition from $\mathbb{P}^1$ to $\mathbb{P}^2$ and θ_m is the inclination angle parameter, which defines the principal direction of the property variation relative to the x_1-axis. The generalized FGM interpolation with arbitrary grading orientations has been detailed in Ref. [23]. Therefore only a representative grading direction is considered in the present study to focus on the multiphysics structural behavior.

This model permits the calculation of E^{eff}, v^{eff}, κ^{eff}, β^{eff} and γ^{eff} at any required point based on the properties of the two constituent materials and how they are mixed. In the fundamental analyses, these effective material properties are assumed to be independent of temperature.

3. Fundamental formulation modeling of thermo-mechanical-pressure multi-material optimization

The design domain Ω is discretized into N_e polygonal elements. Corresponding to these elements, an original design variable matrix is defined as:

$$\overline{\boldsymbol{\psi}} = \begin{Bmatrix} \boldsymbol{\psi}_1 & \boldsymbol{\psi}_2 & \boldsymbol{\psi}_3 \end{Bmatrix} \in \mathbb{R}^{N_e \times m-1} \tag{32}$$

where $\boldsymbol{\psi}_k = \begin{Bmatrix} \psi_k^1 & \psi_k^2 & \dots & \psi_k^{N_c} \end{Bmatrix}^T \in \mathbb{R}^{N_c \times 1}$ is the vector containing the k-th original design variables; m corresponding to the total number of material phases, including the void.

To suppress checkerboarding phenomena, this study applies a density filtering method [5]. This filter performs a transformation to modify the original density values ψ_i^e. The result of this process is the vector of filtered design variables, denoted as $\overline{\boldsymbol{\alpha}} = \begin{Bmatrix} \alpha_1 & \alpha_2 & \alpha_3 \end{Bmatrix} \in \mathbb{R}^{N_e \times m-1}$ (with $\boldsymbol{\alpha}_k$ being the k-th filtered variable):

$$\alpha_k^e = \frac{\sum w_{eg}^k \psi_k^g}{\sum w_{eg}^k} \tag{33}$$

where $w_{eg}^k = \max\left\{0, R - r_{ge}\right\}$ is a weight function, R is the filter radius, and r_{ge} is the distance between the centroid of element g (an element in the neighborhood of e) and the centroid of element e; and ψ_k^g is the k-th original design variable of element g.

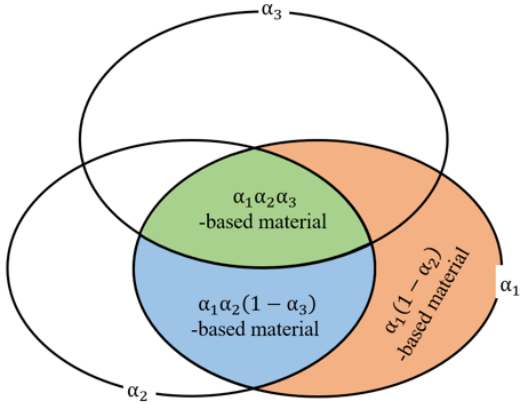

Figure 3. Visual representation of the generalized SIMP three-material interpolation using three design variables

3.1. Material interpolation

In the coupled thermo-mechanical multi-material topology optimization problem, the material distribution is determined via design variables at each finite element. The physical properties requiring interpolation include the constitutive matrix ($\mathbf{D}^{int}$), the thermal conductivity matrix ($\mathbf{D}_{th}^{int}$), and the general thermal stress coefficient (γ^{int}). Let Ψ represent any property tensor within the set $\left\{\mathbf{D}^{int}, \mathbf{D}_{th}^{int}, \gamma^{int}\right\}$.

At any point within the design domain, the effective material property $\Psi(\boldsymbol{\alpha})$ is expressed through the design variable vector $\boldsymbol{\alpha}$ as follows [18]:

$$\Psi(\boldsymbol{\alpha}) = \sum_{t=1}^{m} \beta_t(\boldsymbol{\alpha})\, \hat{\Psi}^{m-t+1} \tag{34}$$

where $\hat{\Psi}^m$ represents the property of the void phase, to avoid singularity in numerical calculations, the void properties are assigned a very small value relative to the softest solid material: $\hat{\Psi}^m = \epsilon_c \Psi^s$ (with $\epsilon_c = 10^{-6}$ [18]); $\Psi^1, \Psi^2, \dots, \Psi^{m-1}$ are the properties of the solid materials and $\beta_t(\boldsymbol{\alpha})$ is the weighting

component, which determines the material distribution based on the generalized SIMP method, is defined recursively as follows:

$$\beta_t(\boldsymbol{\alpha}) = \left[1 - (\alpha_t - \alpha_t \delta_{tm})^{p_j}\right] \prod_{j=1}^{t-1} \left(\alpha_j\right)^{p_j} \tag{35}$$

where p_j is the penalization parameter corresponding to the design variable of the j-th layer and δ_{tm} denotes the Kronecker delta function of indices t and m.

For the specific problem in this study consisting of 3 phases (2 solids and 1 void), the specific interpolation equations for each physical field are derived from the general formula above as follows:

$$\begin{aligned}
\mathbf{D}^{int}\left(\alpha_1^e, \alpha_2^e\right) &= \left(\alpha_1^e\right)^{p_1}\left(\alpha_2^e\right)^{p_2}\mathbf{D}^1 + \left(\alpha_1^e\right)^{p_1}\left(1 - \left(\alpha_2^e\right)^{p_2}\right)\mathbf{D}^2 + \epsilon_c\left(1 - \left(\alpha_1^e\right)^{p_1}\right)\mathbf{D}^s \\
\mathbf{D}_{th}^{int}\left(\alpha_1^e, \alpha_2^e\right) &= \left(\alpha_1^e\right)^{p_1}\left(\alpha_2^e\right)^{p_3}\mathbf{D}_{th}^1 + \left(\alpha_1^e\right)^{p_1}\left(1 - \left(\alpha_2^e\right)^{p_3}\right)\mathbf{D}_{th}^2 + \epsilon_c\left(1 - \left(\alpha_1^e\right)^{p_1}\right)\mathbf{D}_{th}^s \\
\gamma^{int}\left(\alpha_1^e, \alpha_2^e\right) &= \left(\alpha_1^e\right)^{p_1}\left(\alpha_2^e\right)^{p_3}\gamma^1 + \left(\alpha_1^e\right)^{p_1}\left(1 - \left(\alpha_2^e\right)^{p_3}\right)\gamma^2 + \epsilon_c\left(1 - \left(\alpha_1^e\right)^{p_1}\right)\gamma^s
\end{aligned} \tag{36}$$

Note that in this study, the penalization parameters are set differently for mechanical and thermal properties: $p_1 = p_2 = 3$ for mechanical stiffness, and $p_3 = 1$ for thermal properties [43, 46, 47]; however, the influence of p_2 is also investigated. A similar logical framework applies to the formulation of problems involving one and three solid phases.

The formulation is completed by substituting the interpolated properties into the finite element Eqs. (6), (10), and (18). This yields the final, design-dependent elemental matrices used for the optimization process:

$$\begin{aligned}
\mathbf{K}_{th}^e(\overline{\boldsymbol{\alpha}}) &= \int_{\Omega_e} \mathbf{B}_{th}^{eT}\mathbf{D}_{th}^{int}(\overline{\boldsymbol{\alpha}})\mathbf{B}_{th}^e\, dxdy \\
\mathbf{K}^e(\overline{\boldsymbol{\alpha}}) &= \int_{\Omega_e} \mathbf{B}^{eT}\mathbf{D}^{int}(\overline{\boldsymbol{\alpha}})\mathbf{B}^e\, dxdy \\
\mathbf{F}_\epsilon^e(\overline{\boldsymbol{\alpha}}) &= \gamma^{int}(\overline{\boldsymbol{\alpha}})\mathbf{C}^e\left(\mathbf{T}^e - T_{ref}\mathbf{1}^e\right)
\end{aligned} \tag{37}$$

3.2. Problem statement

This problem is formulated as a mathematical optimization problem. The objective is to find the material distribution (via the variables $\boldsymbol{\alpha}_1$ and $\boldsymbol{\alpha}_2$) that minimizes the structural compliance. The goal is to minimize the objective function C [48]:

$$C = (\mathbf{F}_\epsilon + \mathbf{F}_t - \mathbf{HP})^T\mathbf{U} \tag{38}$$

where $\mathbf{F}_t$ is the global fixed traction load vector; $\mathbf{H}$ is the global pressure-to-force conversion matrix; and $\mathbf{U}$ is the global displacement vector.

The design must satisfy the following thermal, pressure, and mechanical equilibrium equations for the system:

$$\begin{aligned}
\mathbf{K}_{th}\mathbf{T} &= \mathbf{F}_{th} \\
\left(\mathbf{K}_p + \mathbf{K}_{Dp}\right)\mathbf{P} &= 0 \\
\mathbf{KU} &= \mathbf{F}_\epsilon + \mathbf{F}_t - \mathbf{HP}
\end{aligned} \tag{39}$$

The optimization process is subject to constraints on the total allowable volume of each material. Specifically, the total volumes of k-th material must not exceed the prescribed limits V_k^f [19]:

$$h_2^k(\overline{\boldsymbol{\alpha}}) = \sum_e v_e\left[1 - \boldsymbol{\alpha}_{m-k+1}^e\left(1 - \delta_{(m-1)(m-k)}\right)\right]\prod_{j=1}^{m-k}\boldsymbol{\alpha}_j^e - V_k^f\sum_e v_e \le 0, \forall k = \overline{1, m-1} \tag{40}$$

where v_e is the volume of a polygonal element.

4. Sensitivity analysis

To address the optimization problem, this study employs a gradient-based method, the Method of Moving Asymptotes (MMA [49]). A core requirement of MMA is the availability of sensitivity analyses (derivatives) of the objective function (C) and the constraint functions (h_2^k). First, the sensitivities with respect to the original design variables (ψ) are calculated from the filtered variables (α) via the chain rule:

$$\frac{\partial \chi}{\partial \psi_i^j} = \sum_c \frac{\partial \chi}{\partial \alpha_i^e} \frac{\partial \alpha_i^e}{\partial \psi_i^j} \tag{41}$$

where χ is an arbitrary function (C or h_2^k). The following subsections will elaborate on the calculation of the derivative $\partial\chi/\partial\alpha_i^e$ for each case.

4.1. Sensitivity for the compliance

To find the derivative of the compliance (C), we utilize the adjoint method [48]. First, an augmented Lagrangian function is constructed by combining the compliance (C) with three adjoint vectors ($\mathbf{\Lambda}_{th}, \mathbf{\Lambda}_m, \mathbf{\Lambda}_p$) and the equilibrium Eq. (39):

$$\begin{aligned} C = \; & (\mathbf{F}_\epsilon + \mathbf{F}_t - \mathbf{HP})^T \mathbf{U} + \mathbf{\Lambda}_{th}^T (\mathbf{K}_{th}\mathbf{T} - \mathbf{F}_{th}) \\ & + \mathbf{\Lambda}_m^T (\mathbf{KU} - \mathbf{F}_\epsilon - \mathbf{F}_t + \mathbf{HP}) + \mathbf{\Lambda}_p^T \left(\mathbf{K}_p + \mathbf{K}_{Dp}\right)\mathbf{P} \end{aligned} \tag{42}$$

Taking the total derivative of C with respect to the filtered variable α_i^e, we obtain Eq. (43). This expression contains the terms $\partial U/\partial\alpha_i^e$, $\partial T/\partial\alpha_i^e$ and $\partial P/\partial\alpha_i^e$, which are components that are very difficult to compute:

$$\begin{aligned} \frac{\partial C}{\partial \alpha_i^e} = \; & \frac{\partial \mathbf{F}_\epsilon^T}{\partial \alpha_i^e}\mathbf{U} + \mathbf{\Lambda}_{th}^T \frac{\partial \mathbf{K}_{th}}{\partial \alpha_i^e}\mathbf{T} + \mathbf{\Lambda}_m^T \left(\frac{\partial \mathbf{K}}{\partial \alpha_i^e}\mathbf{U} - \frac{\partial \mathbf{F}_\epsilon}{\partial \alpha_i^e}\right) \\ & + \mathbf{\Lambda}_p^T \left(\frac{\partial \mathbf{K}_p}{\partial \alpha_i^e} + \frac{\partial \mathbf{K}_{Dp}}{\partial \alpha_i^e}\right)\mathbf{P} + \left[(\mathbf{F}_\epsilon + \mathbf{F}_t - \mathbf{HP})^T + \mathbf{\Lambda}_m^T \mathbf{K}\right] \frac{\partial \mathbf{U}}{\partial \alpha_i^e} \\ & + \left(\mathbf{U}^T \frac{\partial \mathbf{F}_\epsilon}{\partial \mathbf{T}} + \mathbf{\Lambda}_{th}^T \mathbf{K}_{th} - \mathbf{\Lambda}_m^T \frac{\partial \mathbf{F}_\epsilon}{\partial \mathbf{T}}\right) \frac{\partial \mathbf{T}}{\partial \alpha_i^e} \\ & + \left[\mathbf{\Lambda}_m^T \mathbf{H} + \mathbf{\Lambda}_p^T \left(\mathbf{K}_p + \mathbf{K}_{Dp}\right) - \mathbf{U}^T \mathbf{H}\right] \frac{\partial \mathbf{P}}{\partial \alpha_i^e} \end{aligned} \tag{43}$$

The key to the adjoint method is to strategically choose the vectors $\mathbf{\Lambda}$ such that these computationally expensive terms vanish. The adjoint vectors are selected as follows:

$$\begin{aligned} \mathbf{\Lambda}_{th}^T &= -2\mathbf{U}^T \frac{\partial \mathbf{F}_\epsilon}{\partial \mathbf{T}} \mathbf{K}_{th}^{-1} \\ \mathbf{\Lambda}_m &= -\mathbf{U} \\ \mathbf{\Lambda}_p^T &= 2\mathbf{U}^T \mathbf{H} \left(\mathbf{K}_p + \mathbf{K}_{Dp}\right)^{-1} \end{aligned} \tag{44}$$

Upon applying these adjoint vectors to Eq. (43), the expression for the derivative of the compliance C is significantly simplified, depending only on known variables and the derivative of the elemental matrix:

$$\frac{\partial C}{\partial \alpha_i^e} = -\mathbf{U}^{eT} \frac{\partial \mathbf{K}^e}{\partial \alpha_i^e}\mathbf{U}^e + 2\mathbf{U}^{eT} \frac{\partial \mathbf{F}_\epsilon^e}{\partial \alpha_i^e} + \mathbf{\Lambda}_{th}^{eT} \frac{\partial \mathbf{K}_{th}^e}{\partial \alpha_i^e}\mathbf{T}^e + \delta_{1i}\mathbf{\Lambda}_p^{eT} \left(\frac{\partial \mathbf{K}_p^e}{\partial \alpha_1^e} + \frac{\partial \mathbf{K}_{Dp}^e}{\partial \alpha_1^e}\right)\mathbf{P}^e \tag{45}$$

where δ_{1i} is the Kronecker delta; $\mathbf{\Lambda}_{th}^{e}$ and $\mathbf{\Lambda}_{p}^{e}$ stand for the e-th elemental vectors corresponding to global adjoints $\mathbf{\Lambda}_{th}$ and $\mathbf{\Lambda}_{p}$, respectively.

The derivatives of the elemental matrix in Eq. (45) are defined as follows:

$$\begin{aligned}
\frac{\partial \mathbf{K}^{e}}{\partial \alpha_{i}^{e}} &= \int_{\Omega_{e}} \mathbf{B}^{eT} \frac{\partial \mathbf{D}^{int}}{\partial \alpha_{i}^{e}} \mathbf{B}^{e}\, dxdy \\
\frac{\partial \mathbf{F}_{\epsilon}^{e}}{\partial \alpha_{i}^{e}} &= \frac{\partial \gamma^{int}}{\partial \alpha_{i}^{e}} C^{e} \left(\mathbf{T}^{e} - T_{ref}\mathbf{1}^{e}\right) \\
\frac{\partial \mathbf{K}_{\rho}^{e}}{\partial \alpha_{1}^{e}} &= \frac{\partial K}{\partial \alpha_{1}^{e}} \int_{\Omega_{e}} \hat{\mathbf{B}}^{eT} \hat{\mathbf{B}}^{e}\, dxdy \\
\frac{\partial \mathbf{K}_{Dp}^{e}}{\partial \alpha_{1}^{e}} &= \frac{\partial D}{\partial \alpha_{1}^{e}} \int_{\Omega_{e}} \boldsymbol{\phi}^{eT} \boldsymbol{\phi}^{e}\, dxdy \\
\frac{\partial \mathbf{K}_{th}^{e}}{\partial \alpha_{i}^{e}} &= \int_{\Omega_{e}} \mathbf{B}_{th}^{eT} \frac{\partial \mathbf{D}_{th}^{int}}{\partial \alpha_{i}^{e}} \mathbf{B}_{th}^{e}\, dxdy
\end{aligned} \tag{46}$$

The derivatives of the interpolation functions (assuming $p_1 = 3$ and $p_3 = 1$) are given by (2 solids and 1 void):

$$\begin{aligned}
\frac{\partial \mathbf{D}^{int}}{\partial \alpha_{1}^{e}} &= 3\left(\alpha_{1}^{e}\right)^{2}\left(\alpha_{2}^{e}\right)^{p_2}\left(\mathbf{D}^{1} - \mathbf{D}^{2}\right) + 3\left(\alpha_{1}^{e}\right)^{2}\left(\mathbf{D}^{2} - \epsilon_{c}\mathbf{D}^{s}\right) \\
\frac{\partial \mathbf{D}^{int}}{\partial \alpha_{2}^{e}} &= p_2\left(\alpha_{1}^{e}\right)^{3}\left(\alpha_{2}^{e}\right)^{p_2-1}\left(\mathbf{D}^{1} - \mathbf{D}^{2}\right) \\
\frac{\partial \gamma^{int}}{\partial \alpha_{1}^{e}} &= 3\left(\alpha_{1}^{e}\right)^{2}\alpha_{2}^{e}\left(\gamma^{1} - \gamma^{2}\right) + 3\left(\alpha_{1}^{e}\right)^{2}\left(\gamma^{2} - \epsilon_{c}\gamma^{s}\right) \\
\frac{\partial \gamma^{int}}{\partial \alpha_{2}^{e}} &= \left(\alpha_{1}^{e}\right)^{3}\left(\gamma^{1} - \gamma^{2}\right) \\
\frac{\partial K}{\partial \alpha_{1}^{e}} &= -\left(k_{v} - k_{s}\right)\beta_{k}\frac{1 - \tanh\left(\beta_{k}\left(\alpha_{1}^{e} - \eta_{k}\right)\right)^{2}}{\tanh\left(\beta_{k}\eta_{k}\right) + \tanh\left(\beta_{k}\left(1 - \eta_{k}\right)\right)} \\
\frac{\partial D}{\partial \alpha_{1}^{e}} &= h_{s}\beta_{h}\frac{1 - \tanh\left(\beta_{h}\left(\alpha_{1}^{e} - \eta_{h}\right)\right)^{2}}{\tanh\left(\beta_{h}\eta_{h}\right) + \tanh\left(\beta_{h}\left(1 - \eta_{h}\right)\right)} \\
\frac{\partial \mathbf{D}_{th}^{int}}{\partial \alpha_{1}^{e}} &= 3\left(\alpha_{1}^{e}\right)^{2}\alpha_{2}^{e}\left(\mathbf{D}_{th}^{1} - \mathbf{D}_{th}^{2}\right) + 3\left(\alpha_{1}^{e}\right)^{2}\left(\mathbf{D}_{th}^{2} - \epsilon_{c}\mathbf{D}_{th}^{s}\right) \\
\frac{\partial \mathbf{D}_{th}^{int}}{\partial \alpha_{2}^{e}} &= \left(\alpha_{1}^{e}\right)^{3}\left(\mathbf{D}_{th}^{1} - \mathbf{D}_{th}^{2}\right)
\end{aligned} \tag{47}$$

A similar logical framework applies to the formulation of problems involving one and three solid phases.

The detailed expansions of the elemental matrix derivatives with respect to the design variables are straightforwardly obtained using the chain rule on the generalized SIMP interpolation schemes. To maintain conciseness, the explicit mathematical formulations of these derivatives are omitted here but can be found in detail in existing literature [48, 50].

4.2. Sensitivity for the volume constraints

The calculation of sensitivity for the volume constraints (h_1 and h_2) is much more straightforward. Its partial derivatives with respect to the filtered variables α_1^e and α_2^e are defined as follows (2 solids and 1 void):

$$\begin{aligned}
\frac{\partial h_1}{\partial \alpha_1^e} &= v_e \alpha_2^e \\
\frac{\partial h_1}{\partial \alpha_2^e} &= v_e \alpha_1^e \\
\frac{\partial h_2}{\partial \alpha_1^e} &= v_e \left(1 - \alpha_2^e\right) \\
\frac{\partial h_2}{\partial \alpha_2^e} &= -v_e \alpha_1^e
\end{aligned} \tag{48}$$

The formulation for scenarios with one or three solid materials plus a void follows a parallel logic.

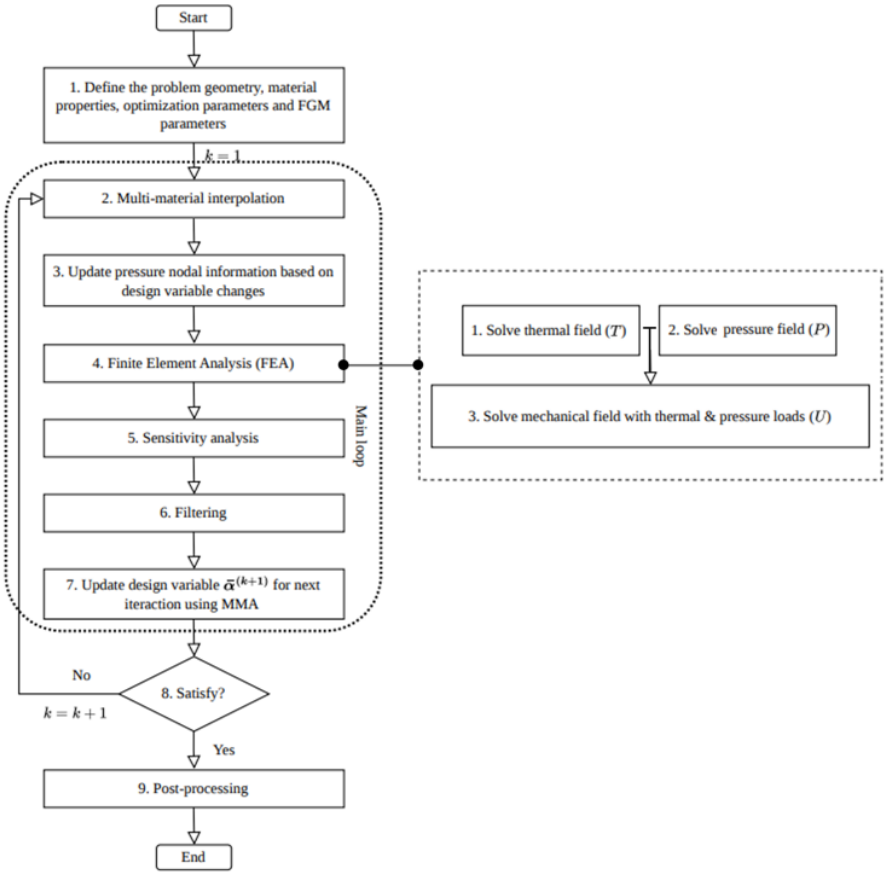

Figure 4. Flowchart of the current method

5. Demonstration examples

This section presents numerical examples to assess the proposed framework's accuracy, robustness, and applicability for heterogeneous materials under coupled multiphysics conditions. Specifically, these studies address the stable sensitivity evaluation of FGMs subjected to simultaneous thermal, mechanical, and design-dependent pressure loads.

The investigations follow a three-stage progression. First, a standard thermo-mechanical problem validates the formulation against benchmark results by Shishir and Tabarraei [47]. Second, design-dependent pressure loading is incorporated and benchmarked against studies by Kumar et al. [42] and Banh et al. [22]. Finally, the framework's full potential is illustrated through FGM topology optimization under a fully coupled thermo-mechanical-pressure setting.

To ensure stability, the iterative process terminates when the maximum difference between consecutive steps falls below 10^{-3} for the objective function ($\|C^{(k)} - C^{(k-1)}\|_\infty$) and 10^{-2} for the design variables ($\|\overline{\alpha}^{(k)} - \overline{\alpha}^{(k-1)}\|_\infty$) over two iterations, or upon reaching 2500 iterations. Finally, post-processing techniques are used to extract the FGM geometry.

5.1. Example 1

A bi-clamped rectangular beam 60×20 dimensionless units is investigated (Fig. 5). The structure is subjected to a concentrated mechanical load $F = 1$ at the bottom edge midpoint (black arrow), a uniform heat flux $q_0 = 3$ across the top surface (red arrows), and a heat sink $T_{sink} = 0$ at the bottom boundary (green highlight). The domain is discretized into 7500 quadrilateral (Q4) elements with a filter radius of $R = 1.2$. Notably, the uppermost element layer is assigned a thermal conductivity 100 times the maximum value.

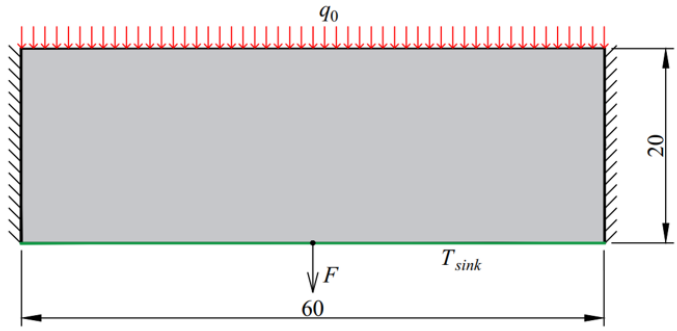

Figure 5. Geometry, load and boundary conditions of a bi-clamped rectangular beam

The objective is to minimize compliance under a 40% total solid volume constraint. For multi-material configurations, this volume is equally partitioned (20% each) between the Red and Blue phases. Heterogeneous properties vary along the y-direction using parameters $\chi = 20$ and $\theta_m = \pi/2$. Detailed material properties are listed in Table 1 and Table 2.

Table 1. Properties of homogeneous materials for Example 1

Material properties	Single material (red)	Double materials	
		1st material (red)	2nd material (blue)
Young's modulus	$E_r = 1$	$E_r = 2$	$E_b = 1$
Poisson's ratio	$v_r = 0.3$	$v_r = 0.3$	$v_b = 0.3$
Thermal conductivity	$k_r = 1$	$k_r = 2$	$k_b = 1$
Thermal expansion coefficient	$\beta_r = 5 \times 10^{-4}$	$\beta_r = 2 \times 10^{-4}$	$\beta_b = 5 \times 10^{-4}$

The optimization results between the coarse Q4 mesh [47] and the proposed fine mesh are shown in Fig. 6 and Fig. 7. Both provide a similar, arch-like topology, providing algorithmic stability. In the multi-material problem, the proposed approach successfully inhibits intermediate phases and a sharp boundary is drawn between two solid materials for practical manufacturability. Additionally,

the two-material structure exhibits a lower degree of compliance compared to the single material baseline, showing better structural stiffness. Moreover, as the normalized temperature plot indicates, material is distributed away from the heat source to mitigate thermal expansion stresses, confirming the framework's precision in coupled thermo-mechanical problems.

Table 2. Properties of heterogeneous materials properties for Example 1

Material properties	Single material (red)		Double material (red and blue)		
	1st component	2nd component	1st material (blue)		2nd material (red)
			1st component	2nd component	
Young's modulus	$E_r^1 = 1$	$E_r^2 = 2$	$E_b^1 = 1$	$E_b^2 = 1.5$	$E_r = 2$
Poisson's ratio	$v_r^1 = 0.3$	$v_r^2 = 0.3$	$v_b^1 = 0.3$	$v_b^2 = 0.32$	$v_r = 0.3$
Thermal conductivity	$k_r^1 = 1$	$k_r^2 = 2$	$k_b^1 = 1$	$k_b^2 = 3$	$k_r = 2$
Thermal expansion coefficient	$\beta_r^1 = 5 \times 10^{-4}$	$\beta_r^2 = 2 \times 10^{-4}$	$\beta_b^1 = 5 \times 10^{-4}$	$\beta_b^2 = 3 \times 10^{-4}$	$\beta_r = 2 \times 10^{-4}$

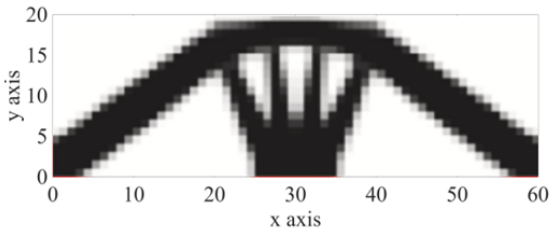

(a) C = 16.37, 1200 Q4 [47]

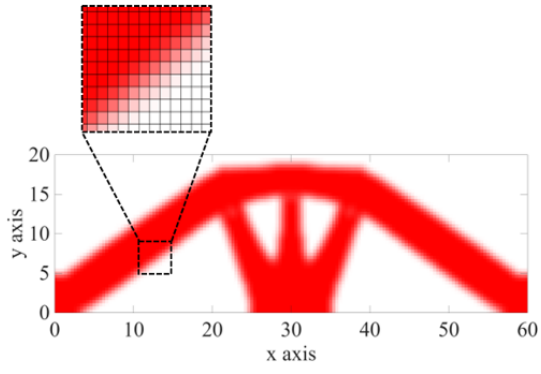

(b) C = 15.69, 7500 Q4

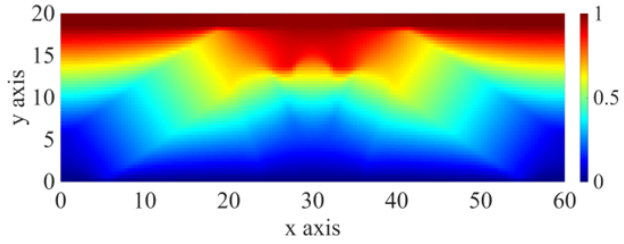

(c) Plot of normalized temperature

Figure 6. Comparison of optimal topologies for single material with different meshes

Fig. 7 elucidates the impact of the material penalty parameter (p_2) on the optimal topology and material distribution within the multi-material design framework. Observations indicate that the employment of a linear penalty scheme ($p_2 = 1$) results in an ambiguous material distribution, characterized by a substantial presence of intermediate density regions at the interface between the Red and Blue phases, which poses significant challenges for fabrication. In contrast, the implementation of a non-linear penalty ($p_2 = 3$) effectively suppresses intermediate phases, yielding sharp and definitive boundaries between the two solid material phases, thereby ensuring practical manufacturability. Given these advantages, $p_2 = 3$ is adopted for the subsequent numerical examples.

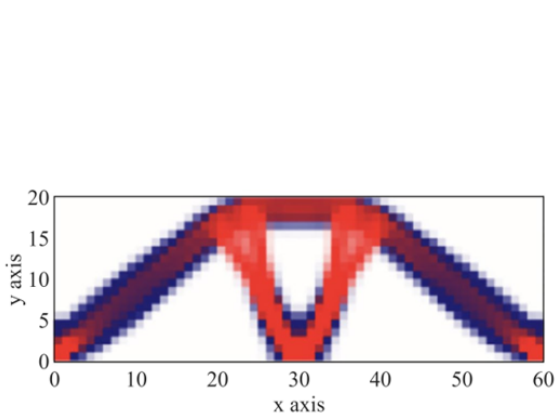

(a) C = 8.88, 1200 Q4 [47]

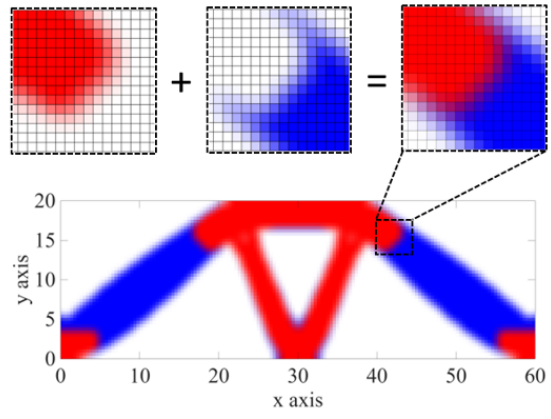

(b) C = 9.06, 7500 Q4

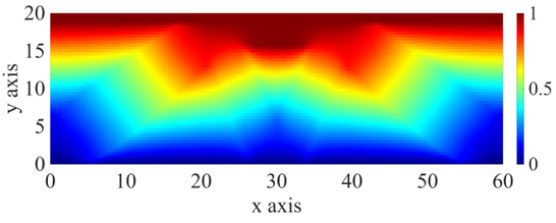

(c) Normalized temperature plot

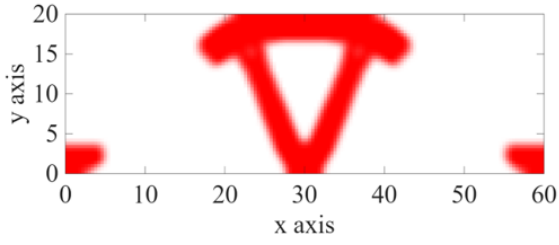

(d) Red material

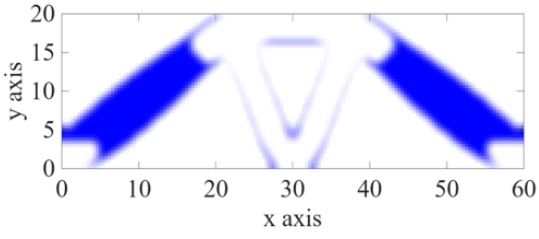

(e) Blue material

Figure 7. Comparison of optimized Topologies for double-material with different meshes

As Fig. 8 and Fig. 9 indicate, the single material design yields the lowest performance due to limited thermal regulation. While the multi-material configuration improves structural stiffness via distinct phase separation, the FGM solution provides better structural efficiency. The FGM design achieves this optimum compromise of stiffness, especially under coupled thermo-mechanical conditions, by employing a smooth thermal gradient and by optimizing the placement of structural materials. The effectiveness and stability of our proposed method is shown in Fig. 10, and both single and multi material designs converge very quickly within 30 iterations, all under strict volume constraints. The multi-material configuration has lower compliance than the single material design, achieving increased structural stiffness and confirming the algorithm's robustness.

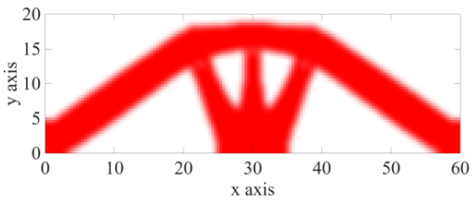

(a) C = 15.69, 7500 Q4, homogeneous material

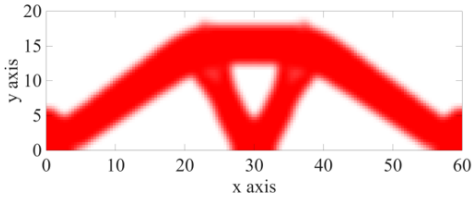

(b) C = 9.89, 7500 Q4, FG material

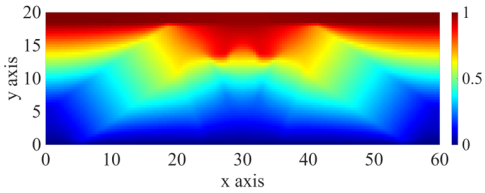

(c) Plot of normalized temperature

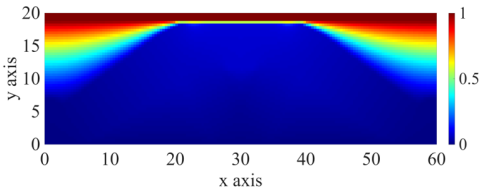

(d) Plot of normalized temperature

Figure 8. Comparison of optimal topologies for single material with FGM case

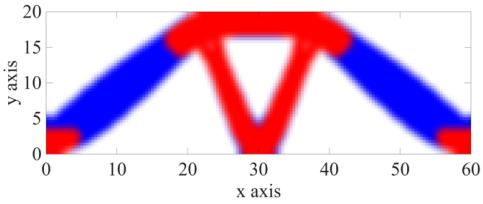

(a) C = 9.06, 7500 Q4, homogeneous material

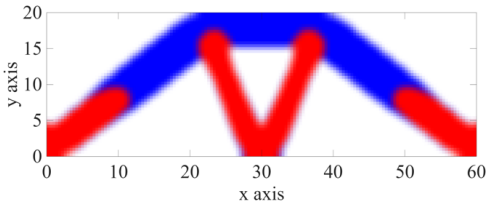

(b) C = 8.11, 7500 Q4, homogeneous and FG materials

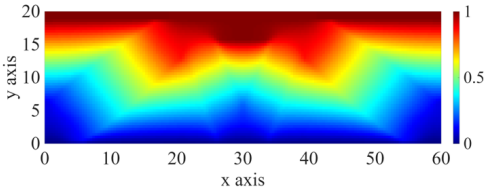

(c) Plot of normalized temperature

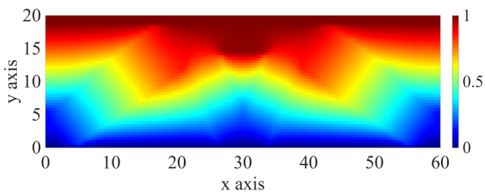

(d) Plot of normalized temperature

Figure 9. Comparison of optimal topologies for double materials with FGM case

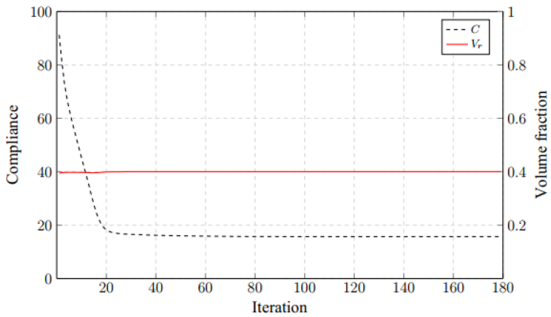

(a) Single homogeneous material

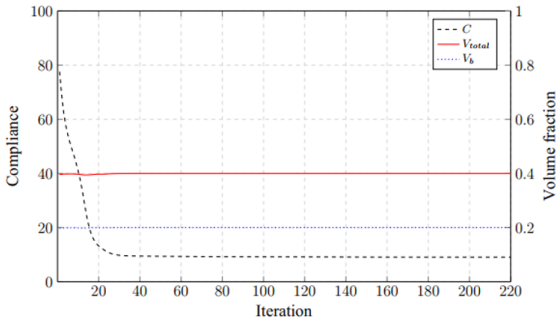

(b) Double homogeneous materials

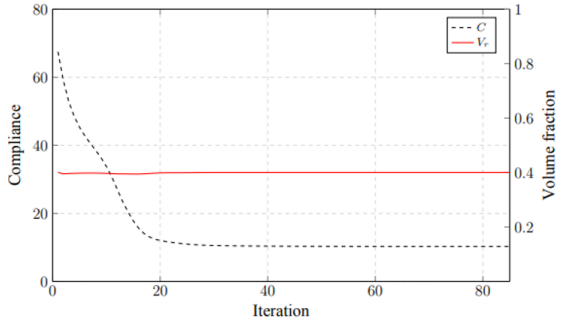

(c) Single FG material

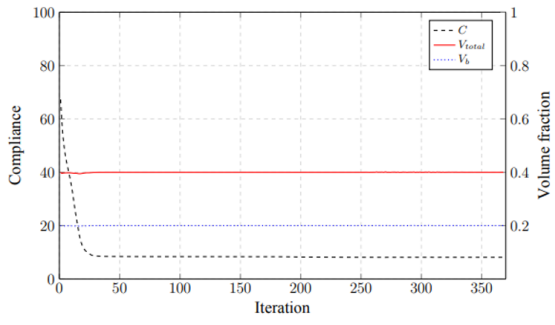

(d) Double homogeneous and FG materials

Figure 10. Evolution of compliances of optimal structures with various amounts of materials and volumes

5.2. Example 2

An arch structure subjected to design-dependent pressure loads is investigated using a mesh of 5000 quadrilateral (Q4) elements. The rectangular design domain (100 m × 50 m) with unit thickness is subjected to a full pressure boundary condition $P_1 = 1$ (cyan arrows) on the top and lateral boundaries, while a zero-pressure condition $P_0 = 0$ (orange highlight) is maintained at the bottom. Detailed displacement boundary conditions are shown in Fig. 11.

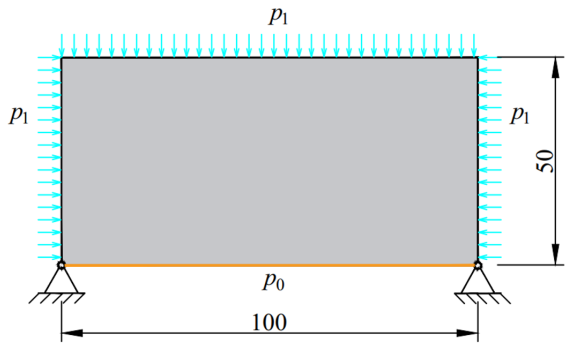

Figure 11. Geometry, load and boundary conditions of the arch structure

Pressure field parameters are set as $\{\beta_k, \eta_k\} = \{12, 0.1\}$ and $\{\beta_h, \eta_h\} = \{12, 0.3\}$. The optimization uses the GMMA solver with a filter radius of $R = 1.5$ m and a 20% total volume limit. Three scenarios are investigated using properties from Table 3: single material (20% Red), homogeneous multi-material (10% Red, 10% Blue), and heterogeneous FGM systems. Beyond the baseline (10% Blue, 10% Red FGM) in Table 4, the study explores two advanced three-material scenarios using properties from Table 5: (1) one FGM phase (Red) with two homogeneous phases (Blue, Green); and (2) two FGM phases (Red, Green) with one homogeneous phase (Blue), with each phase occupying 6.67% volume.

Table 3. Properties of homogeneous materials properties for Example 2

Material properties	Single material	Double materials	
		1st material (red)	2nd material (blue)
Young's modulus (GPa)	$E_r = 70$	$E_r = 70$	$E_b = 122.56$
Poisson's ratio	$v_r = 0.3$	$v_r = 0.3$	$v_b = 0.3$

Results in Fig. 12 and Fig. 13 show high consistency with previous studies by Kumar et al. [42] and Banh et al. [22] for both single and multi material problems. In addition, the switch to a multi material layout may reduce compliance by about 30%, validating the approach and pointing out that it will improve structural efficiency compared to single material designs.

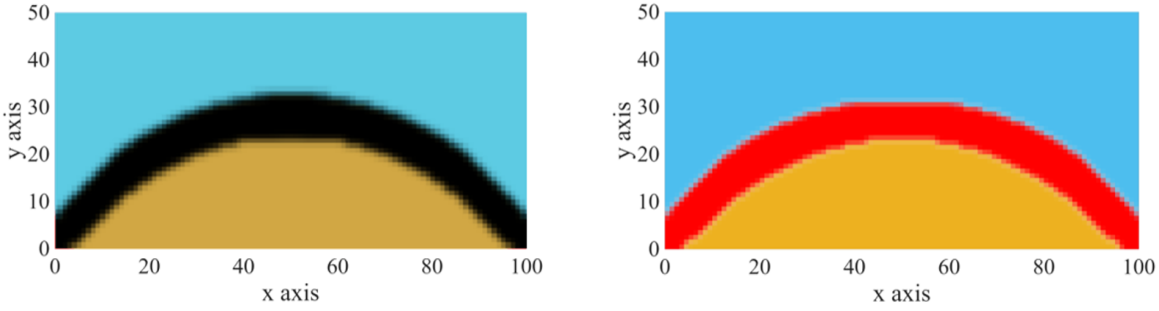

(a) C = 105.48 Nm, Q4 [42] (b) C = 107.38 Nm, Q4

Figure 12. Optimal designs of the arch structure with single material

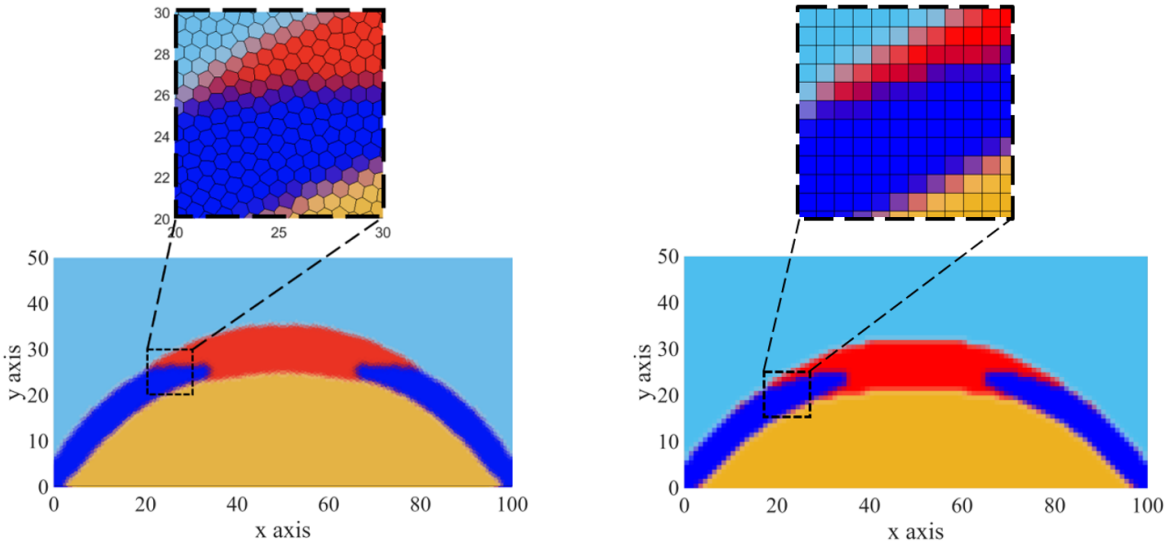

(a) C = 73.80 Nm, PEs [22] (b) C = 75.03 Nm, Q4

Figure 13. Optimal designs of the arch structure with double material

From Fig. 14, FGM gradation direction is found to strongly impact structural performance due to material rearrangement to reinforce weak areas. Due to this, horizontal gradation (FGM2) is an asymmetric topology according to load yielding the minimum compliance. FGM1a (increased stiffness upward) with vertical gradation is superior to FGM1b, because it positions stiffer material at the top of the arch crown to be capable of resisting compressive forces. These findings suggest that the alignment of the material gradient with the stress state maximizes stiffness in structure.

A comparative analysis shows that FGM solutions consistently outperform the alternatives, traditional single and multi material methods throughout both Q4 and PEs discretizations [22]. Unlike uniform (standardized) conventional designs, FGM configurations exploit spatial property differences to minimize compliance effectively. Consequently, these heterogeneous designs lead to a better over-

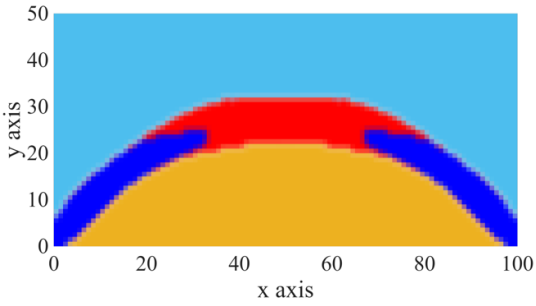

(a) C = 72.77 Nm, Q4, FGM1a

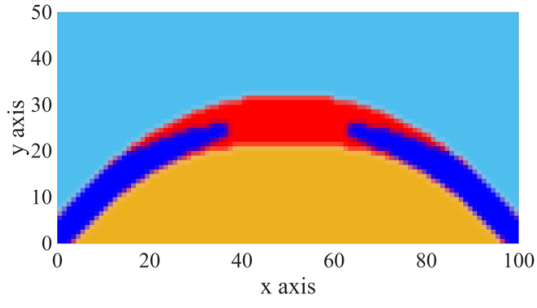

(b) C = 73.48 Nm, Q4, FGM1b

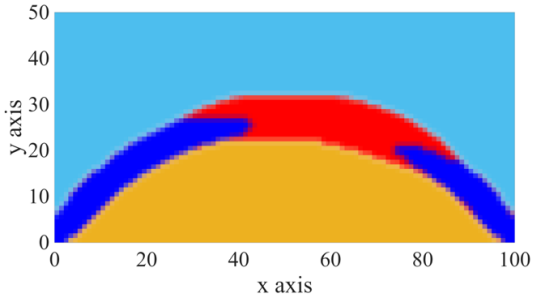

(c) C = 72.58 Nm, Q4, FGM2

Figure 14. Optimal designs of the arch structure with double materials case

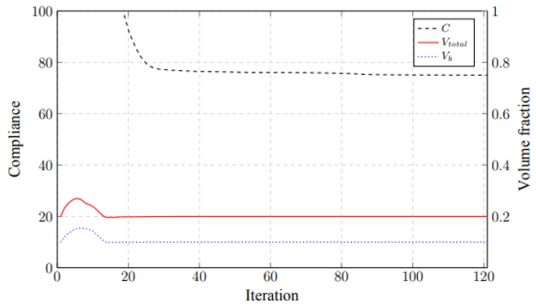

(a) Double homogeneous materials

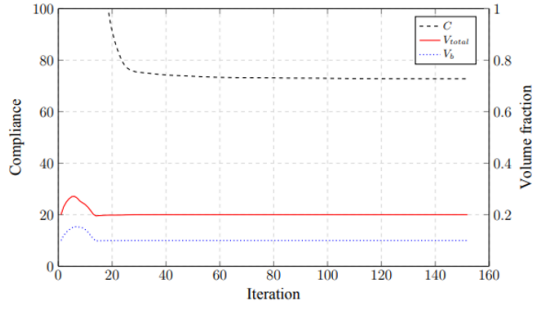

(b) FGM1a

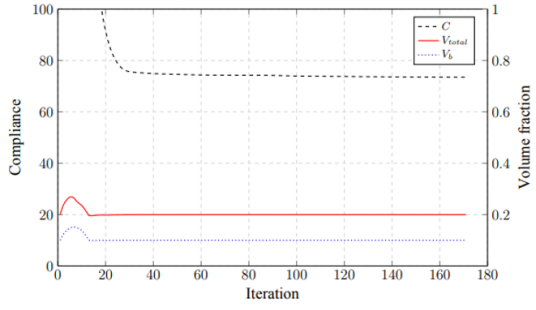

(c) FGM1b

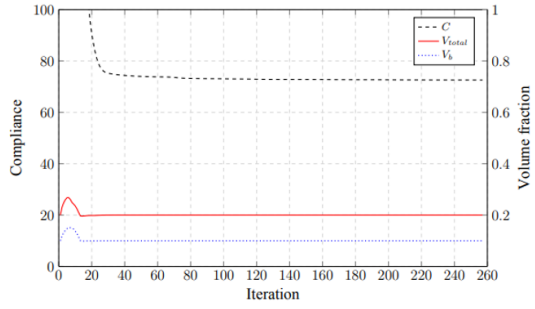

(d) FGM2

Figure 15. Evolution of compliances of optimal structures with various amounts of materials and volumes

all structural stiffness: they prove that material gradients are necessary to optimize performance under challenging loading.

From the variation between Fig. 16 two, the structural efficiency is higher for FGM3a. Moreover, there is also a comparison of Q4 mesh and a 10,000 PEs mesh for FGM3a that confirms that PEs are more accurate and performance improving. The enhanced flexibility of the PEs mesh mitigates numerical instabilities and ensures a more continuous material distribution. Consequently, PEs are adopted as the standard discretization method for the remainder of this study.

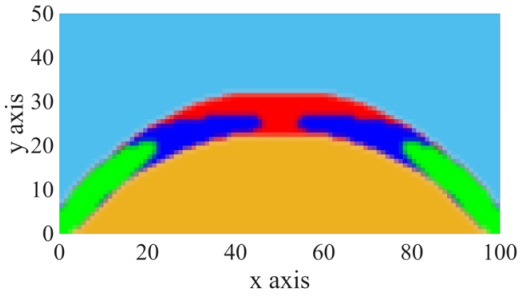

(a) C = 72.29 Nm, Q4, FGM3a

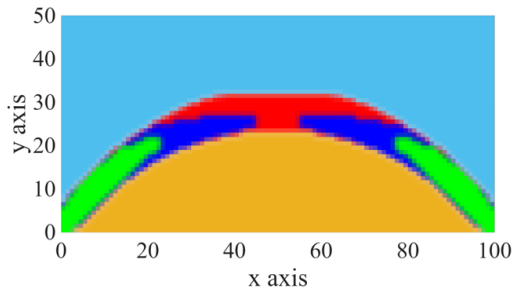

(b) C = 75.57 Nm, Q4, FGM3b

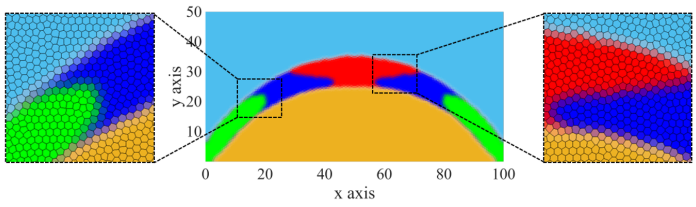

(c) C = 72.18 Nm, PEs, FGM3a

Figure 16. Optimal designs of the arch structure with triple materials case

Table 4. Properties of double materials for Example 2

FG materials			Properties	
			Young's modulus (GPa)	Poisson's ratio
FGM1a $\{\theta_m, \chi\} = \{\pi/2, L_y\}$	Blue material: Ti-6Al-4V		E_b = 122.56	ν = 0.3
	FG-Red material: Vitual material	1st component: Aluminium	E_r^1 = 70	
		2nd component: vitual material	E_r^2 = 80	
FGM1b $\{\theta_m, \chi\} = \{\pi/2, L_y\}$	Blue material: Ti-6Al-4V		E_b = 122.56	
	FG-Red material: Vitual material	1st component: vitual material	E_r^1 = 80	
		2nd component: Aluminium	E_r^2 = 70	

FG materials			Properties	
			Young's modulus (GPa)	Poisson's ratio
FGM2 $\{\theta_m, \chi\} = \{0, L_x\}$	Blue material: Ti-6Al-4V		$E_b = 122.56$	
	FG-Red material: Vitual material	1st component: Aluminium	$E_r^1 = 70$	
		2nd component: vitual material	$E_r^2 = 80$	

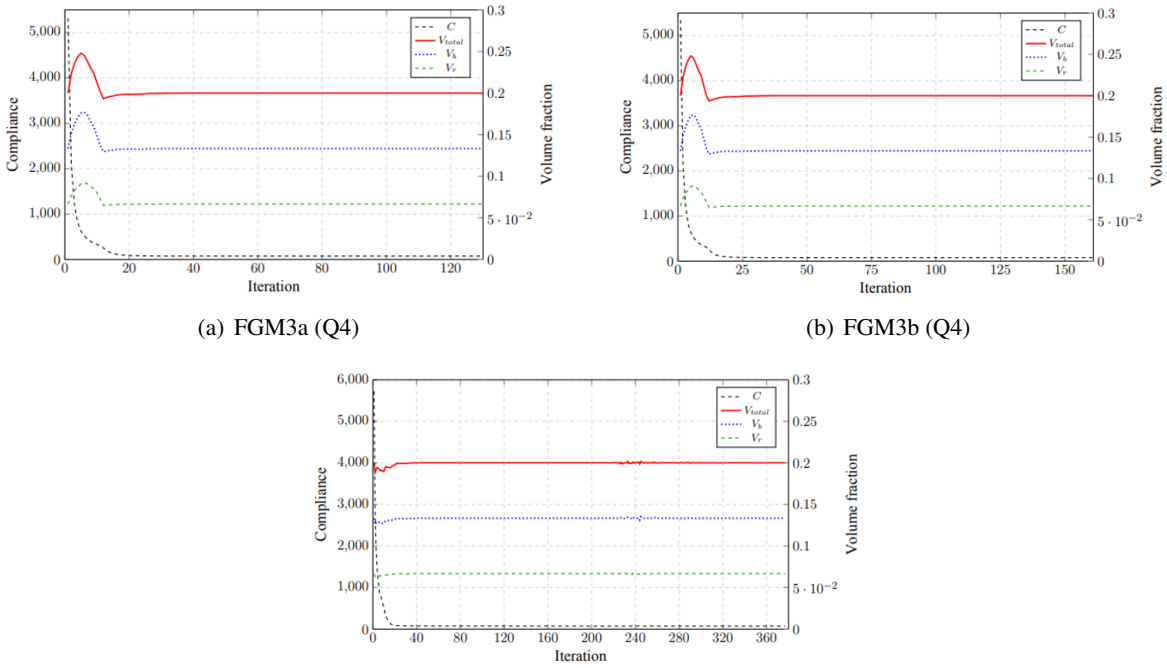

(a) FGM3a (Q4)

(b) FGM3b (Q4)

(c) FGM3a (PEs)

Figure 17. Evolution of compliances of optimal structures with various amounts of materials and volumes

Table 5. Properties of triple materials for Example 2

FG materials			Properties	
			Young's modulus (GPa)	Poisson's ratio
FGM3a $\{\theta_m, \chi\} = \{\pi/2, L_y\}$	FG-Red material: Vitual material	1st component: Aluminium	$E_r^1 = 70$	$v = 0.3$
		2nd component: Vitual material	$E_r^2 = 80$	

FG materials			Properties	
			Young's modulus (GPa)	Poisson's ratio
	Blue material: vitual material		$E_b = 100$	
	Green material: Ti-6Al-4V		$E_g = 122.56$	
FGM3b $\{\theta_m, \chi\} = \{\pi/2, L_y\}$	FG-Red material: Vitual material	1^{st} component: Aluminium	$E_r^1 = 70$	
		2^{nd} component: Vitual material	$E_r^2 = 80$	
	Blue material: vitual material		$E_b = 100$	
	FG-Green material: Vitual material	1^{st} component: Vitual material	$E_g^1 = 110$	
		2^{nd} component: Ti-6Al-4V	$E_g^2 = 122.56$	

5.3. Example 3

This example investigates the topology optimization of a 2D closed planar container, simulating the cross-section of a pressurized water pipeline (Fig. 18). The structure is subjected to an internal pressure load $p_c = 1$ kPa (cyan arrows), while external boundaries maintain a zero-pressure condition (orange outline). Thermally, uniform heat fluxes $q_0 = 10^{-3}$ W/m^2 (red arrows) are applied to the top and bottom edges, with a zero-temperature sink (green highlight) at the inner edges. To enhance heat dissipation, the bottommost element layer is assigned a thermal conductivity 100 times the standard value, with a reference temperature $T_{sink} = 0$.

Pressure field parameters are set as $\eta_k = \eta_h = 0.2$, $\beta_k = 18$, and $\beta_h = 8$. Exploiting symmetry, an L-shaped quarter domain is modeled using 8000 unstructured PEs with symmetric boundary conditions (Fig. 18(c)). The domain is 1 m thick, with edges measuring 160 m (left), 200 m (bottom), 80 m (top), and 80 m (right). The objective is to minimize compliance under mixed thermo-mechanical-pressure loading, using a 3 m filter radius and a 20% total volume limit. For multi-material configurations, this volume is equally partitioned: 10% per phase for two-material systems, and 6.67% per phase for three-material systems. Heterogeneous properties vary along the y-direction using parameters $\chi = 160$ and $\theta_m = \pi/2$. Detailed material properties are listed in Table 6 and Table 7.

The methodology is validated against Banh et al. [48, 50] for single and two material models (Fig. 19 and Fig. 20). Minimal compliance deviation and high geometric consistency between the reference (5000 PEs) and current (8000 PEs) simulations confirm the framework's mesh independence. Extending the algorithm to three-material and hybrid FGM configurations (Fig. 21) reveals that heterogeneous designs thermo-mechanically outperform homogeneous counterparts. Rather than concentrating material at the corners, heterogeneous configurations form vertical struts that enhance stiffness. This design also enhances heat transfer by producing a broader, uniform low-temperature central region that mitigates the localized heat accumulation seen in homogeneous designs.

Finally, Fig. 22 presents each case's compliance and volume fraction convergence histories. These plots validate the stability of algorithms and confirm our proposed method for multi-material and heterogeneous structures optimized under coupled thermo-mechanical-pressure loading.

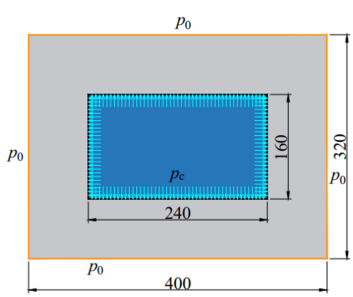

(a) Zero and initial pressure distribution

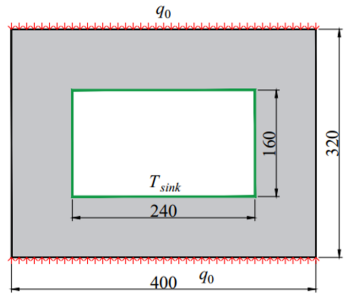

(b) Heat flux and boundary temperature

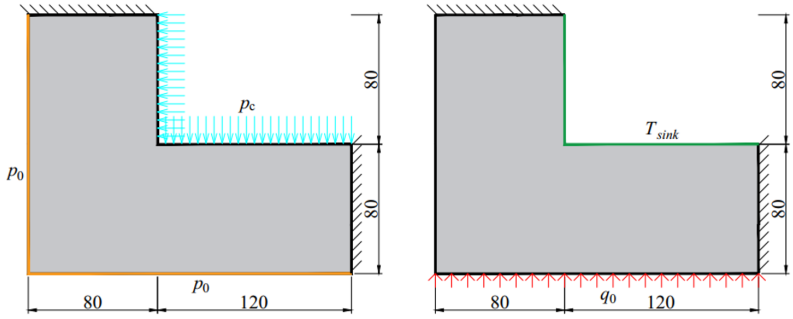

(c) A quarter of the original model with additional simple supports along symmetry planes

Figure 18. Geometry, load, and boundary conditions of a closed planar structure subjected to an internal pressure load

Table 6. Properties of homogeneous materials for example 3

Material properties	Single material (red)	Double materials	
		1st material (red)	2nd material (blue)
Young's modulus (GPa)	$E_r = 70$	$E_r = 70$	$E_b = 122.56$
Poisson's ratio	$v_r = 0.3$	$v_r = 0.3$	$v_b = 0.3$
Thermal conductivity (W/(m.K))	$k_r = 160$	$k_r = 160$	$k_b = 15$
Thermal expansion coefficient	$\beta_r = 22 \times 10^{-6}$	$\beta_r = 22 \times 10^{-6}$	$\beta_b = 9 \times 10^{-6}$

Table 7. Properties of triple materials for example 3

Materials			Properties			
			Young's modulus (GPa)	Poisson's ratio	Thermal conductivity (W/(m.K))	Thermal expansion coefficient ($\times 10^{-6} K^{-1}$)
Homogeneous material	1st red material: Al		$E_r = 70$	$v_r = 0.3$	$\kappa_r = 160$	$\beta_r = 23$
	2nd blue material: Ti-6Al-4V		$E_b = 122.56$	$v_b = 0.3$	$\kappa_b = 15$	$\beta_b = 9$
	3rd green material: SUS304		$E_g = 201$	$v_g = 0.32$	$\kappa_g = 20$	$\beta_g = 17$
Heterogenous material	1st FG-red material:	1st component: Vitual Material	$E_r^1 = 140$	$v_r^2 = 0.3$	$\kappa_r^2 = 150$	$\beta_r^2 = 2$
		2nd component: Al	$E_r^2 = 70$	$v_r^2 = 0.3$	$\kappa_r^2 = 160$	$\beta_r^2 = 23$

Materials			Properties			
			Young's modulus (GPa)	Poisson's ratio	Thermal conductivity (W/(m.K))	Thermal expansion coefficient ($\times 10^{-6} K^{-1}$)
	2^{nd} FG-blue material:	1^{st} component: Vitual Material	$E_b^1 = 200$	$v_b^1 = 0.3$	$\kappa_b^1 = 20$	$\beta_b^1 = 1$
		2^{nd} component: Ti-6Al-4V	$E_b^2 = 122.56$	$v_b^2 = 0.3$	$\kappa_b^2 = 15$	$\beta_b^2 = 9$
	3^{rd} green material:	SUS304	$E_g = 201$	$v_g = 0.32$	$\kappa_g = 20$	$\beta_g = 17$

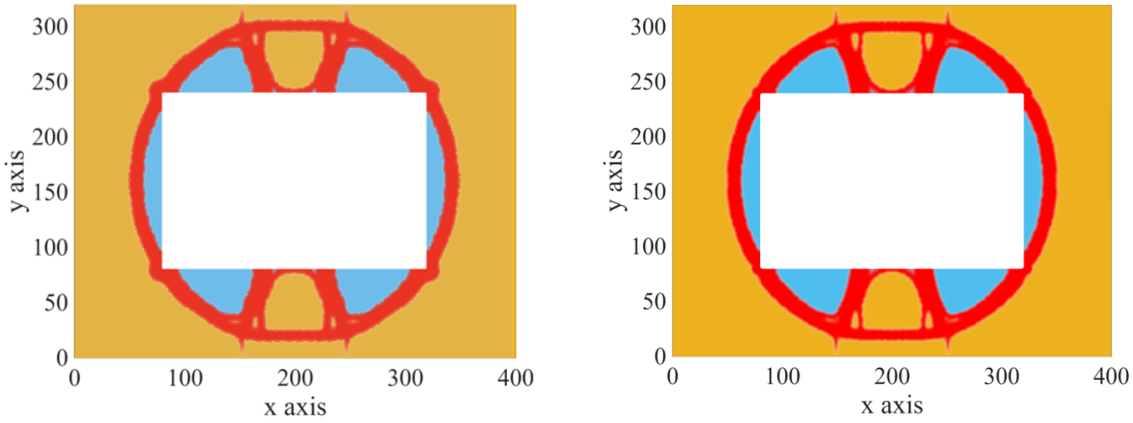

(a) C = 8.09 Nm, 5000 PEs [48] (b) C = 7.76 Nm, 8000 PEs

Figure 19. Optimal designs of closed planar structure with single material

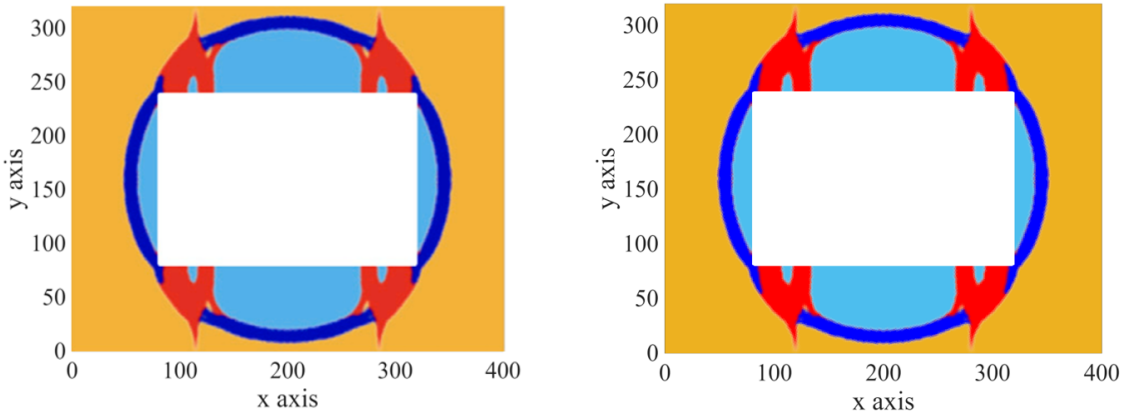

(a) C = 4.27 Nm, 5000 PEs [50] (b) C = 4.28 Nm, 8000 PEs

Figure 20. Optimal designs of closed planar structure with double materials

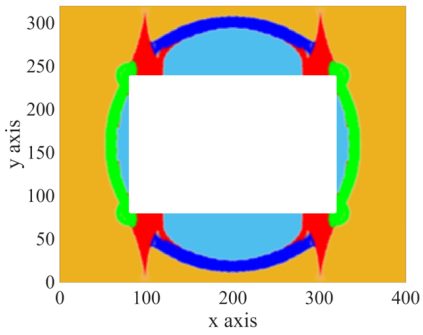

(a) C = 3.62 Nm, 8000 PEs, homogeneous materials

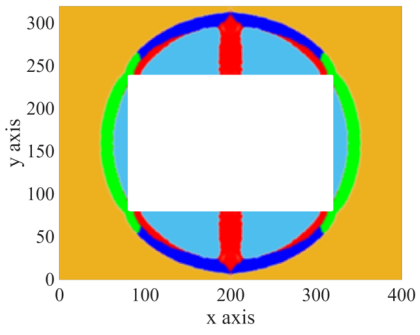

(b) C = 2.09 Nm, 8000 PEs, heterogeneous materials

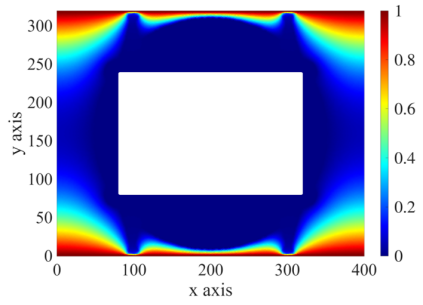

(c) Plot of normalized temperature

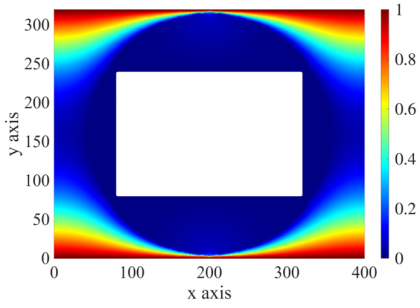

(d) Plot of normalized temperature

Figure 21. Optimal designs of closed planar structure with triple materials

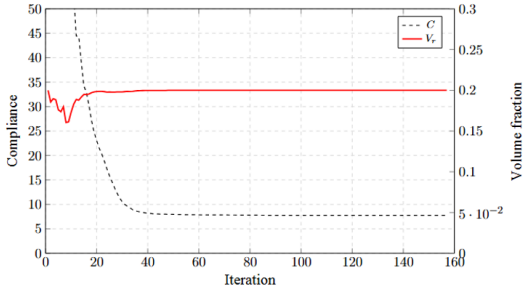

(a) Single homogeneous material

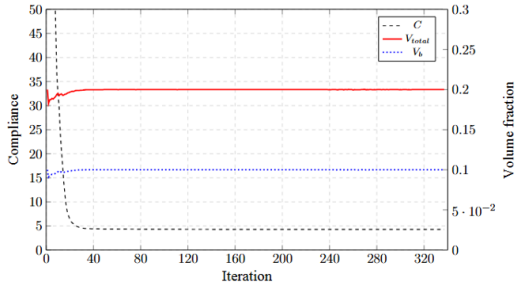

(b) Double heterogeneous materials

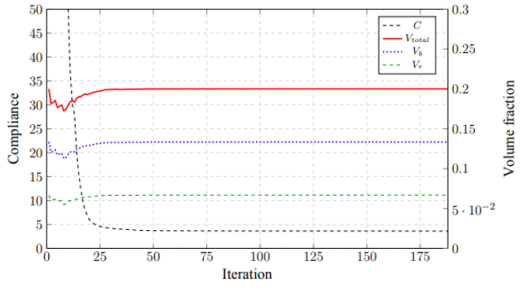

(c) Case 1: triple homogeneous materials

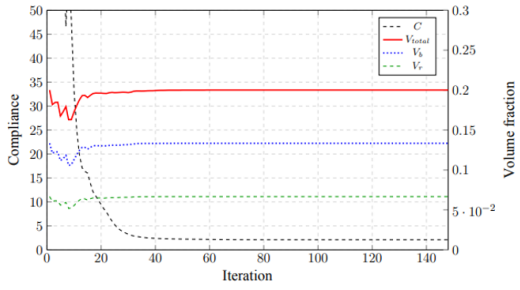

(d) Case 2: triple heterogeneous materials

Figure 22. Evolution of compliances of optimal structures with various amounts of materials and volumes

6. Conclusions

This study has developed a unified topology optimization framework for heterogeneous structures with functionally graded materials under triply coupled thermal-mechanical-pressure multiphysics loading. The primary contribution lies in the consistent integration of heterogeneous material interpolation, design-dependent pressure modeling, and thermoelastic analysis within a single computational framework, enabling a systematic and robust treatment of complex multiphysics interactions in multi material structural design. The proposed framework is validated through a series of numerical examples, which confirm its accuracy, robustness, and numerical stability against established benchmark studies. The results demonstrate that functionally graded designs offer clear advantages over discrete material layouts in multiphysics environments, as continuous material transitions enable improved alignment with combined thermal and mechanical load paths. Future work will focus on extending the framework to three-dimensional applications and incorporating additional design considerations, including buckling, stress, and dynamic constraints, to address more realistic engineering problems.

References

[1] Cheng, K. T., Olhoff, N. (1981). An investigation concerning optimal design of solid elastic plates. *International Journal of Solids and Structures*, 17(3):305–323.

[2] Allaire, G. (2002). *Shape optimization by the homogenization method*. Springer.

[3] Cherkaev, A. (2000). *Variational methods for structural optimization*. Springer.

[4] Tartar, L. (2000). *An introduction to the homogenization method in optimal design*, volume 47-156. Springer Berlin Heidelberg, 47–156.

[5] Bendsøe, M. P., Kikuchi, N. (1988). Generating optimal topologies in structural design using a homogenization method. *Computer Methods in Applied Mechanics and Engineering*, 71(2):197–224.

[6] Hoang, V.-N., Pham, T., Ho, D., Nguyen-Xuan, H. (2021). Robust multiscale design of incompressible multi-materials under loading uncertainties. *Engineering with Computers*, 38(1):875–890.

[7] Tavakoli, R., Mohseni, S. M. (2013). Alternating active-phase algorithm for multimaterial topology optimization problems: A 115-line MATLAB implementation. *Structural and Multidisciplinary Optimization*, 49(4):621–642.

[8] Zhou, S., Wang, M. Y. (2006). Multimaterial structural topology optimization with a generalized Cahn–Hilliard model of multiphase transition. *Structural and Multidisciplinary Optimization*, 33(2): 89–111.

[9] Lieu, Q. X., Lee, J. (2017). Multiresolution topology optimization using isogeometric analysis. *International Journal for Numerical Methods in Engineering*, 112(13):2025–2047.

[10] Lieu, Q. X., Lee, J. (2017). A multi-resolution approach for multi-material topology optimization based on isogeometric analysis. *Computer Methods in Applied Mechanics and Engineering*, 323:272–302.

[11] Nguyen, M. N., Bui, T. Q. (2022). Multi-material gradient-free proportional topology optimization analysis for plates with variable thickness. *Structural and Multidisciplinary Optimization*, 65(3):75.

[12] Zuo, W., Saitou, K. (2016). Multi-material topology optimization using ordered SIMP interpolation. *Structural and Multidisciplinary Optimization*, 55(2):477–491.

[13] Liu, P., Luo, Y., Kang, Z. (2016). Multi-material topology optimization considering interface behavior via XFEM and level set method. *Computer Methods in Applied Mechanics and Engineering*, 308:113–133.

[14] Wang, Y., Luo, Z., Kang, Z., Zhang, N. (2015). A multi-material level set-based topology and shape optimization method. *Computer Methods in Applied Mechanics and Engineering*, 283:1570–1586.

[15] Cai, K., Cao, J., Shi, J., Liu, L., Qin, Q. H. (2015). Optimal layout of multiple bi-modulus materials. *Structural and Multidisciplinary Optimization*, 53(4):801–811.

[16] Li, D., Kim, I. Y. (2018). Multi-material topology optimization for practical lightweight design. *Structural and Multidisciplinary Optimization*, 58(3):1081–1094.

[17] Banh, T. T., Lieu, Q. X., Lee, J., Kang, J., Lee, D. (2023). A robust dynamic unified multi-material topology optimization method for functionally graded structures. *Structural and Multidisciplinary Optimization*, 66(4).

[18] Banh, T. T., Lieu, Q. X., Kang, J., Ju, Y., Shin, S., Lee, D. (2023). A novel robust stress-based multimaterial topology optimization model for structural stability framework using refined adaptive continuation method. *Engineering with Computers*, 40(2):677–713.

[19] Banh, T. T., Shin, S., Kang, J., Zhang, J., Lee, D. (2024). Comprehensive multi-material topology optimization for stress-driven design with refined volume constraint subjected to harmonic force excitation. *Engineering with Computers*, 40(4):2651–2680.

[20] Sigmund, O. (2001). Design of multiphysics actuators using topology optimization – Part II: Two-material structures. *Computer Methods in Applied Mechanics and Engineering*, 190(49-50):6605–6627.

[21] Banh, T. T., Lee, D. (2018). Multi-material topology optimization design for continuum structures with crack patterns. *Composite Structures*, 186:193–209.

[22] Banh, T. T., Shin, S., Kang, J., Lee, D. (2024). Frequency-constrained topology optimization in incompressible multi-material systems under design-dependent loads. *Thin-Walled Structures*, 196:111467.

[23] Banh, T. T., Luu, N. G., Lieu, Q. X., Lee, J., Kang, J., Lee, D. (2024). Multiple bi-directional fgms topology optimization approach with a preconditioned conjugate gradient multigrid. *Composite Structures*, 41: 47–56.

[24] Zhuang, C., Xiong, Z., Ding, H. (2010). Topology optimization of multi-material for the heat conduction problem based on the level set method. *Engineering Optimization*, 42(9):811–831.

[25] Wang, M. Y., Chen, S., Wang, X., Mei, Y. (2005). Design of multimaterial compliant mechanisms using level-set methods. *Journal of Mechanical Design*, 127(5):941–956.

[26] Sukumar, N., Tabarraei, A. (2004). Conforming polygonal finite elements. *International Journal for Numerical Methods in Engineering*, 61(12):2045–2066.

[27] Xia, Q., Wang, M. Y. (2008). Simultaneous optimization of the material properties and the topology of functionally graded structures. *Computer-Aided Design*, 40(6):660–675.

[28] Banh, T. T., Kang, J., Shin, S., Lee, D. (2010). Multi-material polygonal topology optimization for functionally graded isotropic and incompressible linear elastic structures. *Composite Structures*, 92(2): 265–274.

[29] Paulino, G. H., Carlos, E., Silva, N. (2005). Design of functionally graded structures using topology optimization. *Materials Science Forum*, 492-493:435–440.

[30] Carlos, E., Silva, N., Paulino, G. (2005). Topology optimization applied to the design of functionally graded material (FGM) structures. 435–440.

[31] Conlan-Smith, C., James, K. A. (2019). A stress-based topology optimization method for heterogeneous structures. *Structural and Multidisciplinary Optimization*, 60(1):167–183.

[32] Silva, R. F., Coelho, P. G., Conde, F. M., Santos, B. R., Oliveira, J. P. (2024). Minimizing the maximum von mises stress of elastic continuum structures using topology optimization and additively manufactured functionally graded materials. *Computers & Structures*, 301:107469.

[33] Hammer, V. B., Olhoff, N. (2000). Topology optimization of continuum structures subjected to pressure loading. *Structural and Multidisciplinary Optimization*, 19(2):85–92.

[34] Bourdin, B., Chambolle, A. (2003). Design-dependent loads in topology optimization. *ESAIM: Control, Optimisation and Calculus of Variations*, 9:19–48.

[35] Chen, B. C., Kikuchi, N. (2001). Topology optimization with design-dependent loads. *Finite Elements in Analysis and Design*, 37(1):57–70.

[36] Yoon, G. H. (2009). Topology optimization for stationary fluid-structure interaction problems using a new monolithic formulation. *International Journal for Numerical Methods in Engineering*, 82(5):591–616.

[37] Yoon, G. H., Jensen, J. S., Sigmund, O. (2006). Topology optimization of acoustic-structure interaction problems using a mixed finite element formulation. *International Journal for Numerical Methods in Engineering*, 70(9):1049–1075.

[38] Sigmund, O., Clausen, P. M. (2007). Topology optimization using a mixed formulation: An alternative way to solve pressure load problems. *Computer Methods in Applied Mechanics and Engineering*, 196 (13-16):1874–1889.

[39] Kumar, P. (2024). Topology optimization of pressure-loaded multi-material structures. *Lecture Notes in Mechanical Engineering*, 339-351:339–351.

[40] Kumar, P., Frouws, J. S., Langelaar, M. (2020). Topology optimization of fluidic pressure loaded structures and compliant mechanisms using the darcy method. *Structural and Multidisciplinary Optimization*, 61(4):1637–1655.

[41] Kumar, P. (2022). Topology optimization of stiff structures under self-weight for given volume using a smooth heaviside function. *Structural and Multidisciplinary Optimization*, 65(4).

[42] Kumar, P. (2023). Topress: A MATLAB implementation for topology optimization of structures subjected to design-dependent pressure loads. *Structural and Multidisciplinary Optimization*, 66(4).

[43] Thurier, P. F., Lesieutre, G. A., Frecker, M. I., Adair, J. H. (2019). A two-material topology optimization method for structures under steady thermo-mechanical loading. *Journal of Intelligent Material Systems and Structures*, 30(11):1717–1726.

[44] Banh, T. T., Nguyen, S. H., Lee, D. (2025). Comprehensive stress-driven multi-material problem for heat-sinking heterogeneous structures. *Composite Structures*, 352:118638.

[45] Almeida, S. R. M., Paulino, G. H., Silva, E. C. N. (2010). Layout and material gradation in topology optimization of functionally graded structures: A global-local approach. *Structural and Multidisciplinary Optimization*, 42(6):855–868.

[46] Nguyen, M. N., Kang, J., Shin, S., Lee, D. (2023). Dynamic-constrained multi-material topology optimization under heat flux and thermal-mechanical loading. *Thin-Walled Structures*, 193:111218.

[47] Shishir, M. I. R., Tabarraei, A. (2024). Multi-materials topology optimization using deep neural network for coupled thermo-mechanical problems. *Computers & Structures*, 291:107218.

[48] Banh, T. T., Lee, D. (2024). Comprehensive polygonal topology optimization for triplet thermo-mechanical-pressure multi-material systems. *Engineering with Computers*, 40(5):3295–3317.

[49] Svanberg, K. (1987). The method of moving asymptotes-a new method for structural optimization. *International Journal for Numerical Methods in Engineering*, 24(2):359–373.

[50] Banh, T. T., Lee, D. (2025). Comprehensive thermoelastic stress-driven approach for thermo-mechanical-pressure multiphysics systems. *International Journal of Mechanical Sciences*, 291-292:110133.